BNL-222709-2022-JAAM

Role of Bimetallic Interactions in the Enhancement of Catalytic CO2 Reduction by a Macrocyclic Cobalt Catalyst

D. E. Polyansky

To be published in "ACS Catalysis"

January 2022

Chemistry Department

Brookhaven National Laboratory

U.S. Department of Energy

USDOE Office of Science (SC), Basic Energy Sciences (BES) (SC-22)

DISCLAIMER

The Role of Bimetallic Interactions in Enhancement of Catalytic CO_2 Reduction by a Macrocyclic Cobalt Catalyst

Dmitry E. Polyansky,*[a] David C. Grills,[a] Mehmed Z. Ertem,[a] Ken T. Ngo[b,§] and Etsuko Fujita[a]

a. Chemistry Division, Brookhaven National Laboratory, Upton, NY 11973-5000, USA.

b. Department of Chemistry, University of Massachusetts Boston, 100 Morrissey Boulevard, Boston, MA 02125, USA.

*Email: dep@bnl.gov

Keywords: CO_2 reduction, catalysis, pulse radiolysis, catalytic mechanism, cobalt macrocycle

Abstract.

The use of two metal centers in a CO_2 reduction catalyst that work together synergistically, with similar or complementary functions, can potentially lead to a significant reduction in overpotential, enhance catalytic activity and/or selectivity, and/or enable access to cascade strategies where each metal center catalyzes a different step in the conversion of CO_2 to a fuel. Here, the bimetallic reactivity of two metal centers has been identified as the primary route for the reduction of CO_2 to CO promoted by the macrocycle, $[Co(HMD)]^{2+}$ (HMD = 5,7,7,12,14,14-hexamethyl-1,4,8,11-tetraazacyclotetradeca-4,11-diene), based on the experimental characterization of all major steps of the proposed catalytic cycle using pulse radiolysis time-resolved IR spectroscopy (PR-TRIR), corroborated by density functional theory (DFT) calculations and IR spectroelectrochemistry (IR-SEC). A bimetallic intermediate is formed *in-situ* from two singly-reduced $[Co(HMD)]^{+}$ species bridged by a CO_2 molecule, and the presence of a coordinating species, e.g., formate anion, appears to assist in the formation of such an intermediate. It has been demonstrated that this reactivity enables access to elementary steps with lower energy requirements, resulting in overall catalysis being kinetically more facile as compared to the mononuclear pathway. A two-step approach that combines chemical reduction followed by PR-TRIR has been successfully used for probing the structure and reactivity of reactive intermediates involved in the advanced stages of a catalytic cycle, which are rarely interrogated using experimental techniques.

Introduction

In the quest for efficient CO_2 reduction catalysis, the cooperative reactivity of two metal centers has been proposed as a promising strategy for improving the catalytic performance of molecular CO_2 reduction catalysts.[1] Moderate to significant enhancements in catalytic rates and turnover numbers for CO_2 reduction have been reported for complexes containing bimetallic Ni,[2] Fe,[3] Co,[4-5] Pd,[6] and Re[7-8] centers compared to their single-metal congeners. However, the mechanistic understanding of such enhancement is still lacking for most systems, with the exception of Re tricarbonyl bipyridine-type catalysts where the formation of a CO_2-bridged complex containing two one-electron-reduced metal centers, i.e., $[Re(dmb)(CO)_3]_2(CO_2)$ (dmb = 4,4′-dimethyl-2,2′-bipyridine, Chart 1A), has been experimentally identified[9] and its stability rationalized by a formal one-electron transfer from each metal center to the bridging CO_2 ligand.[10] The completion of the catalytic cycle was proposed to involve a second CO_2 molecule as an oxide acceptor, resulting in overall formation of CO and CO_3^{2-}.[10] Following these initial findings, a number of Re-based catalysts containing two metal centers bridged by a linker have been prepared[8, 11-15] with the intent to explore multi-metal catalysis. With some enhancements in catalytic current and anodic shifts in onset potentials for catalysis, the only bimetallic intermediate confidently identified was a Re-Re dimer of two singly-reduced sites, which is typically not considered as an active species towards CO_2 reduction.[8, 13-14] Similarly, a series of bimetallic Co complexes have been used for photosensitized CO_2 reduction catalysis and their high performance was attributed to the cooperative effect of two metal centers.[4-5, 16-17] Again, with rare exceptions[4] the catalytic intermediates or kinetics of elementary catalytic steps implicating the involvement of two metal centers in catalysis have not been positively identified.

Chart 1. Examples of bimetallic intermediates formed *in-situ* during CO_2 reduction: (A) $[Re(dmb)(CO)_3]_2(CO_2)$;[9-10] (B) $[(CO_2)Co(HMD)–OC(O)–Co(HMD)(HCO_2)]^+$.[this work] The structure of the parent $[Co(HMD)]^{2+}$ complex studied in this work is also shown in (C)

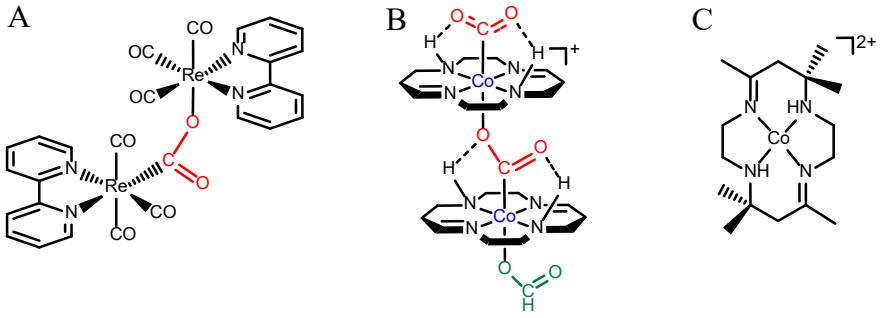

The current study is focused on the identification of reactive bimetallic intermediates (Chart 1B) involved in CO_2 reduction promoted by the macrocyclic $[Co(HMD)]^{2+}$ complex (HMD = 5,7,7,12,14,14-hexamethyl-1,4,8,11-tetraazacyclotetradeca-4,11-diene, Chart 1C). Macrocyclic complexes of Ni and Co were among the first reported molecular electro- and photocatalysts for the reduction of CO_2 to CO,[18-19] with $[\mathbf{Co}]^{2+}$ ($[\mathbf{Co}]^{2+}$ = $[Co(HMD)]^{2+}$) performing as both an electro- and a photocatalyst in aqueous or organic solvents (Table 1). The electrolysis of $[\mathbf{Co}]^{2+}$ in the presence of H_2O catalytically reduces CO_2 and H_2O, producing a H_2/CO mixture. The photolysis of aqueous solutions of $[\mathbf{Co}]^{2+}$, with ascorbate as a sacrificial electron donor (SED) and $Ru(bpy)_3^{2+}$ as a photosensitizer (PS), results in similar products,[19] while in organic solvents, e.g., acetonitrile (CH_3CN)/methanol (CH_3OH) mixtures, with triethylamine (TEA) as a SED and *p*-terphenyl as a PS, the formation of formate was observed, in addition to the abovementioned gases. However, time-resolved UV-vis spectroscopy has shown an efficient formation of the $[Co–CO_2]^+$ adduct in the mixed solvent.[20] While a small amount of Co–H might form by proton transfer from $TEAH^+$ (a product of the known reaction, $TEA^{\bullet+} + TEA \rightarrow (CH_3C^{\bullet}H)N(CH_2CH_3)_2 + TEAH^+$) in the mixed solvent, the observed hydricity of $[\mathbf{Co}–H]^+$ in water indicated that CO_2 insertion into the Co–H bond is highly unfavorable (ΔG_{H^-}(Co–H) = 49 kcal/mol and ($\Delta G_{H^-}(HCO_2^-)$ = 35 kcal/mol).[21] On the other hand, recent reports from the Miller[22-23] and Saouma[24] groups indicate that the binding of anionic species to the metal center following hydride transfer from an M–H species ($M–H + X^- \rightarrow M–X + H^-$) can lead to an increase in the overall driving force for this reaction by 3 – 5 kcal/mol in water and over 10 kcal/mol in organic solvents, which may potentially make CO_2 insertion to $[\mathbf{Co}–H]^+$ thermodynamically favorable. Additionally, complicated reactions involving the strongly reducing *p*-terphenyl radical ($E_{1/2}$ = –2.2 V vs NHE in dimethylamine) or $CO_2^{\bullet-}$ (–1.9 V vs NHE in water) might contribute to the formation of formate.

While the photo- and electrocatalytic performance of $[\mathbf{Co}]^{2+}$ may appear modest compared to other CO_2 reduction catalysts, (e.g., in comparison, TONs of ~10^4 and TOFs of ~ 1 s^{-1} have been reported for Co cryptate complexes),[5] the results reported in Table 1, which are based on previous studies, firmly establish the true catalytic nature of this complex. More importantly, the slow interconversion of catalytic intermediates creates an opportunity for detailed mechanistic studies of the catalytic cycle through isolation of intermediates and their spectroscopic characterization.

Table 1. Electrocatalytic (top) and photocatalytic (bottom) performance of the $[Co(HMD)]^{2+}$ complex towards CO_2 reduction.

Applied Potential (V vs NHE)[a]	Combined TON/TOF (h^{-1})	Products	FE,[b] %	Conditions	Ref
–1.36	82 / 4	CO/H_2, 1/1	93	0.1 M KNO_3 in H_2O/CH_3CN 2:1 (v/v) or H_2O only, [**Co**] = 1.2 × 10^{-3} M	18
–1.36	3 / 2.8	CO/H_2, 2/1	81	0.1 M Et_4NCl in DMF/H_2O 95:5 (v/v); [**Co**] = 1 × 10^{-3} M	19

Photosensitizer, PS	Combined TON/TOF (h^{-1})	Products	Conditions	Ref
$Ru(bpy)_3^{2+}$	100 / na	CO/H_2, 1/4	1 M ascorbate in H_2O; pH 4; [Co] = 8 × 10^{-5} M; [S] = 5 × 10^{-4} M	19
p-terphenyl	>3 / 3	$CO/HCO_2^-/H_2$, 5/1/5	TEOA/CH_3OH/CH_3CN 1/1/4 (v/v); [Co] = 1.7 × 10^{-3} M; [S] = 2 × 10^{-3} M	20
p-terphenyl	>3 / 3	$CO/HCO_2^-/H_2$, 7/1/5	TEA/CH_3OH/CH_3CN 1/1/4 (v/v); [Co] = 1.7 × 10^{-3} M; [S] = 2 × 10^{-3} M	20

a) Potentials reported vs. SCE were converted to NHE by adding 0.24 V; b) FE = Faradaic efficiency

One-electron reduction of $[\mathbf{Co}]^{2+}$ to $[\mathbf{Co}]^{+}$ at room temperature (eq. 1) followed by the addition of CO_2, results in the immediate formation of a pale purple CO_2 adduct (C-bound to the metal center), $[\mathbf{Co}(CO_2)]^{+}$, with λ_{max} at 530 nm (eq. 2). Spectroscopic titration indicates that the five-coordinate 1:1 CO_2 adduct is the dominant cobalt species for solutions containing 0.1-1 atm CO_2

(K_2 = (1.2 ± 0.5) × 10^4 M^{-1} at 25 °C).[25] Introduction of a coordinating species, e.g., a solvent molecule, leads to formation of the six-coordinate complex (eq. 3), with IR bands that are uniquely distinct from the five-coordinate form ($[\mathbf{Co}(CO_2)]^+$ ν_{CO} = 1710 cm^{-1} and $[(S)\mathbf{Co}(CO_2)]^+$ ν_{CO} = 1609 cm^{-1}). A more detailed discussion of the various isomers can be found in SI, Section S0.

$[\mathbf{Co}]^{2+} + e^- \rightleftharpoons [\mathbf{Co}]^+$ $\quad E_{1/2}$ = –1.83 V vs Fc^+/Fc (1)

$[\mathbf{Co}]^+ + CO_2 \rightleftharpoons [\mathbf{Co}(CO_2)]^+$ $\quad K_2 = 10^4\ M^{-1}$ (2)[25]

$[\mathbf{Co}(CO_2)]^+ + S \rightleftharpoons [(S)\mathbf{Co}(CO_2)]^+$ (S = solvent) $\quad K_3 = 0.11\ M^{-1}$ (3)[30]

Dilute solutions of $[\mathbf{Co}(CO_2)]^+$ decay slowly in CO_2-saturated CH_3CN by second order kinetics, $-d[\mathbf{Co}(CO_2)]^+]/dt = k[[\mathbf{Co}(CO_2)]^+]^2$, and k = (1.0 ± 0.1) × 10^{-3} M^{-1} s^{-1} at 23 °C with 0.1–1 atm CO_2. The reaction products are $[\mathbf{Co}]^{2+}$ (100%), CO (30%), H_2 (8%), and $NaHCO_3$ (80%), with the yields based on initial $[\mathbf{Co}]^{2+}$ without formate. The second-order rate law suggests either two $[\mathbf{Co}(CO_2)]^+$ adducts yield CO and CO_3^{2-}/HCO_3^- via electron and oxide transfer reactions, or a disproportionation of binuclear intermediate takes place.[25] In fact, a binuclear species that has the $[\mathbf{Co}–C(OH)O–\mathbf{Co}]^{3+}$ bonding (see Figure 1) has been isolated at –5 °C and the X-ray structure showed a short bond distance between one of the O atoms of the bridged CO_2 and one of the O atoms of the perchlorate anion (2.38 Å), indicating the existence of very strong hydrogen bonding.[25-26] However, involvement of this species in the catalytic mechanism has not been positively identified.

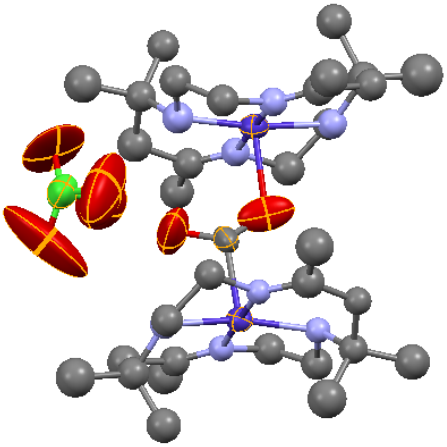

Figure 1. X-ray crystal structure of [**Co**–C(OH)O–**Co**]$^{3+}$ that shows interactions between the bridging C(OH)O ligand and a ClO_4^- counteranion.[25-26] The proton of the bridging C(OH)O group could not be located on a difference Fourier map but its presence is implied by the very short contact between one of its O atoms and an O atom of the ClO_4^- anion (2.38 A, and C–O···O angle of 133.2°).

In this report, we have investigated the reactivity of the singly- and doubly-reduced forms of the [**Co**]$^{2+}$ catalyst and have identified bimetallic reactivity of two metal centers as the primary route for CO_2 reduction, based on experimental characterization of *all major steps* of the proposed catalytic cycle using pulse radiolysis time-resolved IR spectroscopy (PR-TRIR),[27] corroborated by density functional theory (DFT) calculations and IR spectroelectrochemistry (IR-SEC).

Pulse radiolysis, utilizing high-energy electron pulses from an accelerator,[28] is a transient technique that can be applied to both aqueous and organic solvents to rapidly generate strongly reducing radical species, such as the solvated electron (e^-_{solv}), which can in turn reduce dissolved molecules, e.g., catalysts, to produce activated transient intermediates. While pulse radiolysis has been commonly used for studying catalytic intermediates in aqueous solutions,[29] its application in organic solvents, specifically CH_3CN, is complicated by diverse solvent radical ($R^\bullet$) chemistry, originating from the rapid decomposition of radiolytically produced solvent radical cations and excited states (Scheme S0.1 in SI).[30] However, a significant fraction of $R^\bullet$ can be scavenged by the addition of formate anion (HCO_2^-),[30] which results in the formation of $CO_2^{\bullet-}$ radical anion, which is itself a strong reductant (−1.9 V vs. NHE in water). Thus, in CO_2-saturated CH_3CN solutions in

the presence of formate, the combination of e^-_{solv} scavenging by CO_2 and R$^\bullet$ scavenging by HCO_2^-, results in the predominant reducing radical being $CO_2^{\bullet-}$, which can rapidly transfer negative charge to a catalyst molecule.[31]

Results

Spectro-electrochemistry with mid-IR detection (IR-SEC) and Density Funcional Theory calculations for the characterization of singly-reduced intermediates. The electrochemical reduction of [**Co**]$^{2+}$ in dry CH_3CN under a CO_2 atmosphere leads to the formation of [**Co**(CO)]$^+$ via the intermediacy of [**Co**(CO_2)]$^+$ (Figures. S1.2-S1.3), consistent with previous studies.[32-37] The formation of bicarbonate by the protonation of carbonate, even in thoroughly dried CH_3CN (Experimental section), is likely associated with deprotonation of the tetra-*n*-butylammonium (TBA^+) cation of the electrolyte accompanied by the formation of tri-*n*-butylamine and butene by a Hoffman degradation mechanism.[38]

In the presence of $[TBA]^+[H^{13}CO_2]^-$, [**Co**]$^{2+}$ binds formate anion, forming five-coordinate [**Co**($H^{13}CO_2$)]$^+$ (Figures 2A and S2.3, and eq. 4), which upon one-electron reduction releases formate, forming four-coordinate [**Co**]$^+$ (Figures 2B and S2.1, and eq. 5). DFT calculations at the M06-L level of theory predict that the free energy of [**Co**]$^+$ is about 2.9 kcal/mol lower than that of the five-coordinate formate complex (Scheme 1), which agrees well with experimental voltammetry data. The use of ^{13}C-labeled formate red-shifts the carboxyl C=O stretch (from $\nu_{C=O}$ = 1607 cm^{-1} in $H^{12}CO_2^-$ to $\nu_{C=O}$ = 1560 cm^{-1} in $H^{13}CO_2^-$), thus opening the spectroscopic window around 1600 cm^{-1} for observation of the species of interest.

$$[\mathbf{Co}]^{2+} + HCO_2^- \rightleftharpoons [\mathbf{Co}(HCO_2)]^+ \quad (4)$$

$$[\mathbf{Co}(HCO_2)]^+ + e^- \rightleftharpoons [\mathbf{Co}]^+ + HCO_2^- \qquad E_p = -1.7 \text{ V vs } Fc^+/Fc \quad (5)$$

$$[\mathbf{Co}(CO_2)]^+ + HCO_2^- \rightleftharpoons [\mathbf{Co}(CO_2)(HCO_2)] \qquad K_6 = 325 \text{ M}^{-1} \quad (6)$$

Scheme 1. Energetics of singly- and doubly-reduced intermediates of [Co]$^{2+}$ that are generated during CO_2 reduction in the presence of formate, predicted by DFT calculations at the M06-L level of

theory[39] in conjunction with the SMD continuum solvation model[40] for acetonitrile. Free energy changes are in units of kcal/mol and electrochemical potentials are shown in V vs. Fc^+/Fc. Only the most stable and relevant species are presented. The complete structure of the complex is shown in insert and for all future representation of the macrocycle methyl groups and protons are omitted unless they are involved in a reaction step.

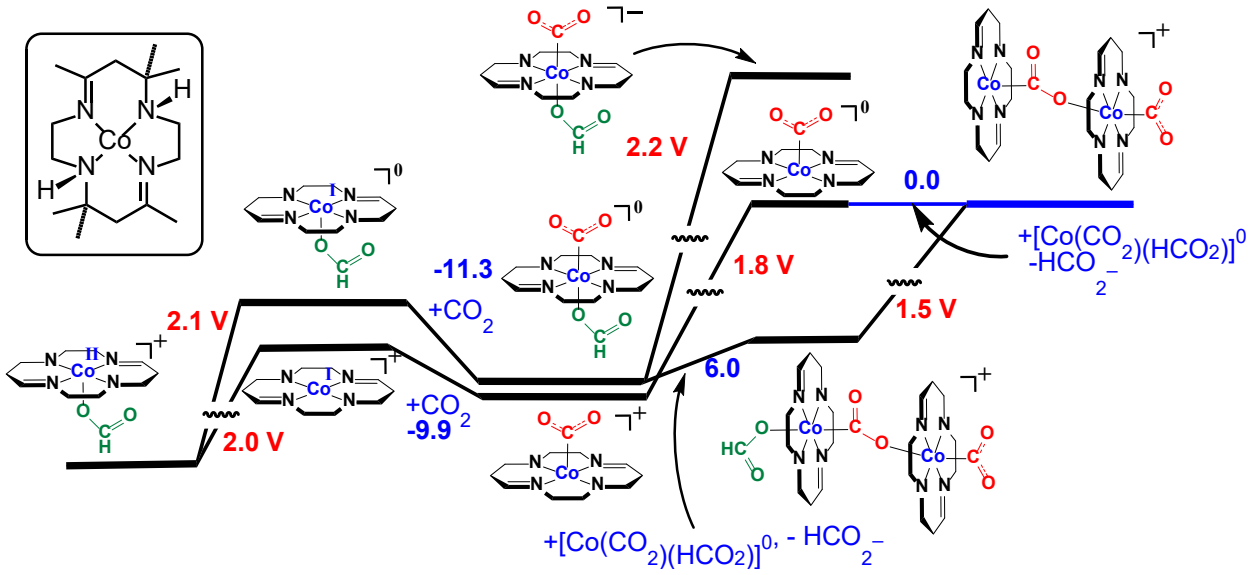

In the presence of formate and CO_2, one-electron reduction of $[\mathbf{Co}(H^{13}CO_2)]^+$ results in the formation of six-coordinate $[\mathbf{Co}(CO_2)(H^{13}CO_2)]$ (Figure 2C). The bands at $\nu_{C=O}$ = 1600 cm^{-1} and $\nu_{C=O}$ = 1224 cm^{-1} were assigned to the antisymmetric and symmetric stretching modes of bound CO_2 in $[\mathbf{Co}(CO_2)(H^{13}CO_2)]$. These assignments were confirmed by the reduction of $[\mathbf{Co}(H^{13}CO_2)]^+$ in the presence of $^{13}CO_2$, resulting in a red shift of the C=O vibrational frequencies of bound CO_2 (Figure 2D). The band at 1575 cm^{-1} was assigned to the bound ^{13}C-labeled formate in $[\mathbf{Co}(CO_2)(H^{13}CO_2)]$. Six-coordinate $[\mathbf{Co}(CO_2)(H^{13}CO_2)]$ exists in equilibrium with five-coordinate $[\mathbf{Co}(CO_2)]^+$ ($\nu_{C=O}$ = 1710 cm^{-1}), with an equilibrium constant of $K_6 \sim 325$ M^{-1} for the addition of HCO_2^- to $[\mathbf{Co}(CO_2)]^+$ (Figures S2.4–S2.5 and eq. 6). Thus, in solutions containing ca. 50 mM $[TBA]^+[HCO_2]^-$, the six-coordinate species is predominant. The predicted energetics of formate binding to $[\mathbf{Co}(CO_2)]^+$, ΔG = 1.5 kcal/mol, is only ca. 4.5 kcal/mol less favorable compared to the value estimated from the experimentally determined equilibrium constant (Scheme 1). This is reasonable given the difficulty in predicting the entropy term for bringing two

ionic species together and other uncertainties associated with using approximate density functionals and continuum solvation to model reactions of transition metal-based complexes.

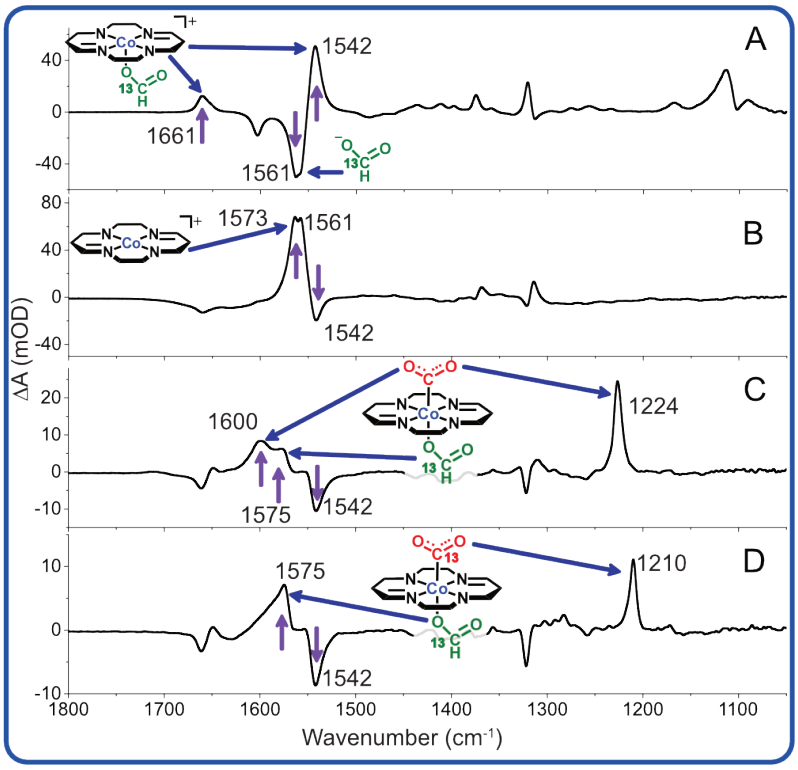

Figure 2. (A) difference spectra of [**Co**]$^{2+}$ in dry CD_3CN in the presence of 50 mM [TBA]$^+$[$H^{13}CO_2$]$^-$ with baseline taken against [TBA]$^+$[$H^{13}CO_2$]$^-$; (B) IR-SEC difference spectra measured during electrochemical reduction of [**Co**]$^{2+}$ in dry CD_3CN containing 0.1 M [TBA]$^+$[PF_6]$^-$ and 50 mM [TBA]$^+$[$H^{13}CO_2$]$^-$ under a N_2 atmosphere at an applied potential of –1.64 V vs. Fc^+/Fc; (C) same as B, but under a CO_2 atmosphere. The extinction coefficient of the 1224 cm^{-1} band is estimated to be ~ 950 ± 150 M^{-1} cm^{-1}; (D) same as B, but under $^{13}CO_2$. See SI Section S2 for more details. Purple arrows indicate the direction of the signal change during electrolysis (e.g., formation – arrow up, and consumption – arrow down).

Interestingly, the IR spectra of the species formed after electrochemical reduction of [**Co**]$^{2+}$ in the presence of formate and CO_2 vary with the initial concentration of the metal complex (Figure 3A). These variations can be rationalized by the presence of both monometallic and bimetallic forms of the CO_2 adduct, i.e., [**Co**(CO_2)($H^{13}CO_2$)], [($^{HB}CO_2$)**Co**–OC(O)–**Co**($H^{13}CO_2$)]$^+$, and [(CO_2)**Co**–OC(O)^{HB}–**Co**($H^{13}CO_2$)]$^+$, by comparing experimental spectra with those predicted by theory (Figures 3B – 3D and S2.8). The two bimetallic structures predicted by DFT calculations

contain one CO_2 molecule and one formate ion as ligands of the Co metal centers, with either the peripheral CO_2 or the bridging CO_2 being hydrogen bonded to an HMD ligand, as denoted by "HB" in the structural formulae. While the computed free energy of both bimetallic isomers is almost identical, both were found to be the most stable structures compared to other combinations of bridging formate or CO_2 species (see SI section S2 for more details). Infrared spectra of [**Co**$(CO_2)(H^{13}CO_2)$] and [$(^{HB}CO_2)$**Co**–OC(O)–**Co**$(H^{13}CO_2)]^+$ exhibit similar C=O stretching frequencies around 1575 cm^{-1}, corresponding to the bound formate ion, while this vibration is slightly blue shifted to 1583 cm^{-1} for the $[(CO_2)$**Co**–OC(O)^{HB}–**Co**$(H^{13}CO_2)]^+$ isomer. The C=O frequency of the bound CO_2 ligand varies significantly between [**Co**$(CO_2)(H^{13}CO_2)$] and both isomers of $[(CO_2)$**Co**–OC(O)–**Co**$(H^{13}CO_2)]^+$. The prominent increase of IR absorption at ca. 1650 cm^{-1} and the red shift of the 1542 cm^{-1} bleach in Figure 3A are consistent with the formation of $[(CO_2)$**Co**–OC(O)^{HB}–**Co**$(H^{13}CO_2)]^+$, while the growth of a 1630 cm^{-1} peak is due to a contribution from $[(^{HB}CO_2)$**Co**–OC(O)–**Co**$(H^{13}CO_2)]^+$. The calculations at the M06-L level indicate that the formation of bimetallic $[(CO_2)$**Co**–OC(O)–**Co**$(HCO_2)]^+$ from two [**Co**$(CO_2)(HCO_2)$] molecules is slightly uphill by ca. 6.0 kcal/mol, consistent with the observed predominance of the monometallic species at low complex concentrations (Scheme 1).

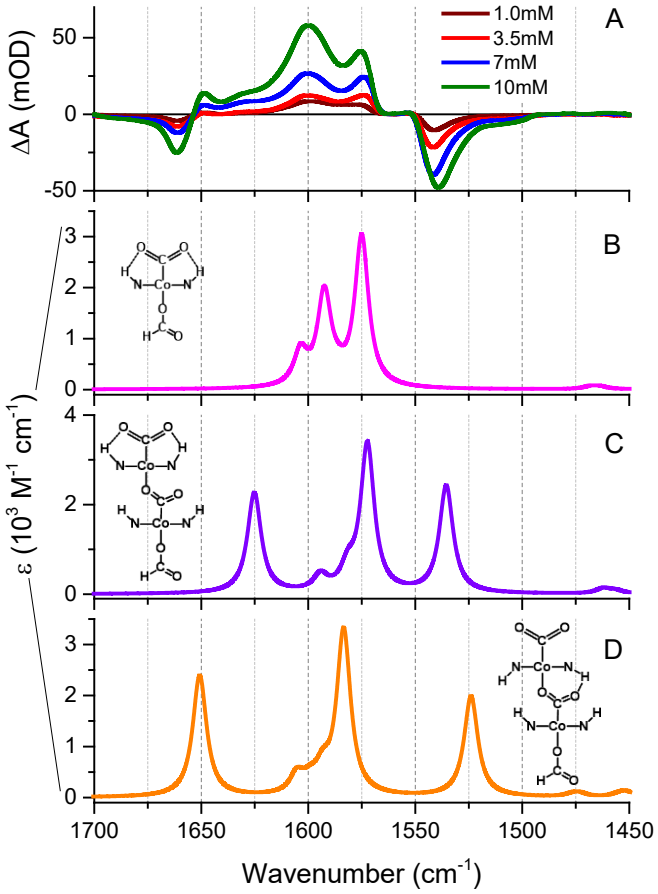

Figure 3. (A) IR-SEC difference spectra measured during electrochemical reduction of various concentrations of $[\mathbf{Co}]^{2+}$ (1 – 10 mM) in dry CD_3CN containing 0.1 M $[TBA]^+[PF_6]^-$ and 50 mM $[TBA]^+[H^{13}CO_2]^-$ under a CO_2 atmosphere at an applied potential of –1.64 V vs. Fc^+/Fc. IR spectra predicted by DFT calculations of: (B) $[\mathbf{Co}(CO_2)(H^{13}CO_2)]$; (C) $[(^{HB}CO_2)\mathbf{Co}–OC(O)–\mathbf{Co}(H^{13}CO_2)]^+$; (D) $[(CO_2)\mathbf{Co}–OC(O)^{HB}–\mathbf{Co}(H^{13}CO_2)]^+$. HB denotes a hydrogen bonding interaction with the HMD ligand. IR frequencies of theoretical spectra are scaled by a factor of 0.934.

Pulse radiolysis with time-resolved mid-IR detection for the characterization of doubly-reduced intermediates. In order to examine the reactivity of the doubly-reduced intermediates, which are expected to be highly unstable, we have employed a strategy whereby a chemically prepared singly-reduced complex is subjected to pulse radiolysis for the rapid addition of a second electron. Specifically, we prepared the six-coordinate, singly-reduced $[\mathbf{Co}(CO_2)(HCO_2)]$ complex

by anaerobic mixing of various concentrations (ca. 1 – 7 mM) of $[\mathbf{Co}]^{+}$ (prepared by Na/Hg chemical reduction of $[\mathbf{Co}]^{2+}$) with solutions of CO_2 and $[TBA]^{+}[HCO_2]^{-}$ in dry CH_3CN on a timescale of < 10 s, during which the degradation of the CO_2 adduct is minimal. As a result of mixing, the final concentrations of CO_2 and $[TBA]^{+}[HCO_2]^{-}$ are 70 mM and 50 mM, respectively, ensuring that $CO_2^{\bullet-}$ will be the only reducing species present after pulse radiolysis (Scheme 1).[30] The reaction of $CO_2^{\bullet-}$ with $[\mathbf{Co}(CO_2)(HCO_2)]$ or $[(CO_2)\mathbf{Co}–OC(O)–\mathbf{Co}(HCO_2)]^{+}$ is expected to proceed by outer-sphere electron transfer, since both complexes are coordinatively saturated and are not capable of binding another ligand. Following pulse radiolysis, these one-electron reductions have been monitored at 1224 cm^{-1}, which corresponds to the symmetric stretching mode of the bound CO_2 in both complexes and does not overlap with other IR bands (Figure 4B). A bi-exponential function provides the best fit for the decay of the 1224 cm^{-1} band (Figure 4D), and both observed rates are found to depend on the initial concentration of the Co complex, with rate constants of 6.3×10^7 M^{-1} s^{-1} (Figure 4F) and 3.8×10^4 M^{-1} s^{-1} (Figure 4H). Concomitant with the fast component of the 1224 cm^{-1} decay, new absorption features which are blue and red shifted relative to the bleach are formed (Figure 4B). These new transient features decay with an observed rate of ca. 55 s^{-1} at 2 mM Co concentration (Figure S3.1). Finally, the appearance of a new band at 1917 cm^{-1} (Figure 4A) is observed, which is characteristic of the CO stretching vibration in $[\mathbf{Co}(CO)]^{+}$.[34] The growth of this band is bi-exponential (Figure 4C), with the faster rate (2.8×10^4 s^{-1}) being independent of the initial Co concentration (Figure 4E), and the slower rate exhibiting dependence on the starting concentration of the metal complex, resulting in a rate constant of 3.4×10^4 M^{-1} s^{-1} (Figure 4G). Using extinction coefficients of $[\mathbf{Co}(CO)]^{+}$ (1590 M^{-1} cm^{-1})[34] and $[\mathbf{Co}(CO_2)(HCO_2)]$ (950 M^{-1} cm^{-1}, see Figure 2C), the absorbances in Figure 4 can be converted to concentrations. The amount of $[\mathbf{Co}(CO)]^{+}$ produced upon the completion of all transient changes is found to be about half of the consumed $[\mathbf{Co}(CO_2)(HCO_2)]$ (Figures 4C and 4D). For example, for the highest concentration of $[\mathbf{Co}(CO_2)(HCO_2)]$, about 42 μM of the complex is consumed, while ca. 19 μM of $[\mathbf{Co}(CO)]^{+}$ is formed.

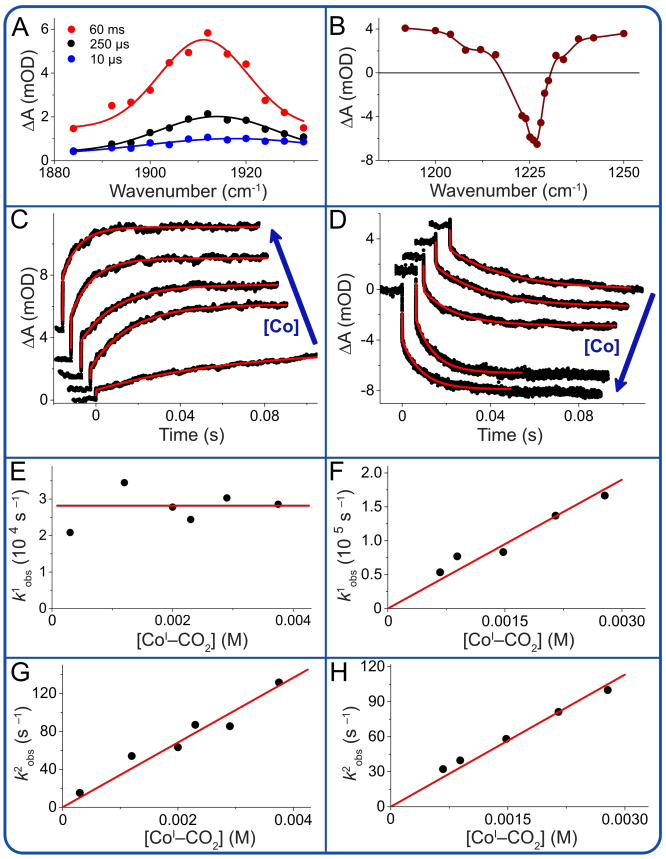

Figure 4. Data collected after pulse radiolysis of rapidly mixed solutions of $[\mathbf{Co}]^{+}$ and CO_2 (70 mM after mixing) and $[TBA]^{+}[HCO_2]^{-}$ (50 mM after mixing) in dry CH_3CN. IR spectral evolution in the 1900 cm^{-1} region (A) and IR spectrum in the 1225 cm^{-1} region at a 5 ms time delay (B) following the electron pulse. Kinetic traces and their bi-exponential fits (red lines) at various concentrations of Co complex at 1917 cm^{-1} (C) and 1224 cm^{-1} (D). Arrows indicate an increase in Co complex concentration. Observed rates and their linear fits (red lines) as a function of concentration of Co complex at 1917 cm^{-1} (fast component – E, slow component – G) and at 1224 cm^{-1} (fast component – F, slow component – H).

Photocatalytic CO_2 reduction under conditions relevant to spectroscopic studies. The photocatalytic activity of $[\mathbf{Co}]^{2+}$ under conditions similar to those used in IR-SEC or pulse radiolysis studies has been examined in the presence of *p*-terphenyl as a PS and TEA as a sacrificial electron donor, similar to the approach described previously.[20] The photochemical mode of catalysis was chosen over an electrochemical approach in an attempt to alleviate strong binding between CO ($K_{eq} \sim 10^8$)[32] and the reduced Co center in the $[\mathbf{Co}(CO)]^{+}$ species, which was identified as one of the intermediates formed during catalysis. We anticipated that a photoexcitation of this

species would facilitate the release of CO to solution and ultimately into the gas phase for detection. Photocatalytic experiments have been carefully designed to avoid significant accumulation of CO gas in the solution and headspace, while providing long catalytic timescales (see Experimental Section for details). Photolysis has been performed at 1 mM and 4 mM of $[\mathbf{Co}]^{2+}$ in the presence of 50 mM $[TBA]^+[HCO_2]^-$ or $[TBA]^+[PF_6]^-$, resulting in the generation of a CO/H_2 mixture in ca. 1/5 ratio. A comparison of CO generation under various conditions is shown in Figure 5 and complete sets of gas evolution data are shown in Figs. S4.1-S4.3. The source of produced hydrogen most likely originates from the decomposition of TEA^+ radical cation, which reacts with another TEA molecule and produces Et_3NH^+ and $Et_2NC^{\bullet}HCH_3$.[20] The accumulation of relatively acidic Et_3NH^+ during the course of photolysis triggers H_2 evolution pathway, which competes with CO_2 reduction. A control experiment in the absence of CO_2, but with 50 mM $[TBA]^+[HCO_2]^-$, results in very little CO formation (Fig. S4.4A), which most likely originates from formate decomposition as it reacts with oxidizing radicals produced during photolysis. The amount of CO derived from formate is significantly smaller than the enhanced yield of CO observed upon substitution of $[PF_6]^-$ with $[HCO_2]^-$ under a CO_2 atmosphere (Fig. S4.4.B), which indicates that formate anion is not the source of evolved CO during CO_2 reduction.

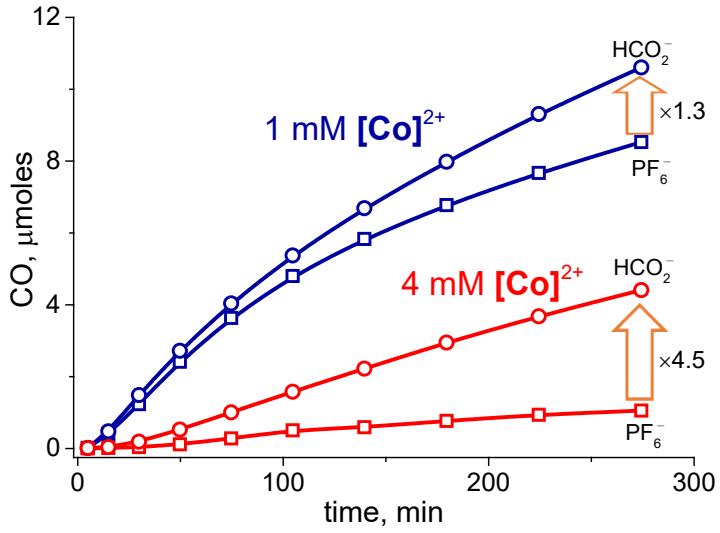

Figure 5. Photocatalytic CO_2 reduction to CO by $[\mathbf{Co}]^{2+}$ in dry CH_3CN with 1 mM *p*-terphenyl and 0.1 M TEA under filtered (> 300 nm) Xe lamp illumination. The concentration of $[\mathbf{Co}]^{2+}$ was 1 mM (dark blue) or 4 mM (red) in the presence of 50mM $[TBA]^+[HCO_2]^-$ (circles) or $[TBA]^+[PF_6]^-$ (squares). The enhancement of CO yields in the presence of formate is shown with orange arrows.

The impact of formate anion on CO yields is more prominent at higher concentration of $[\mathbf{Co}]^{2+}$, where the bimetallic intermediate is formed in appreciable amounts, as evident from the IR-SEC or PR kinetic data discussed above. The overall lower yields of CO at higher concentration of $[\mathbf{Co}]^{2+}$ are not surprising owing to the competitive light absorption by the catalyst and *p*-terphenyl sensitizer in the 250 – 330 nm range. Nevertheless, a relative comparison of yields of CO production points to ca. 1.3× enhancement at 1 mM catalyst concentration and ca. 4.5× increase at 4 mM of catalyst upon substitution of PF_6^- ion by formate. While the total yields of catalysis products may not directly report on any particular step of a catalytic cycle, their magnitudes reflect the overall efficiency of catalysis, especially in comparison to competing side reactions leading to catalyst degradation, which reduces the yield of desired products. The release of CO from the stable $[\mathbf{Co}(CO)]^+$ species appears to be the rate limiting step in overall CO evolution, which limits the assessment of catalytic rates under different catalysis conditions.

Discussion

Collectively, the IR spectroelectrochemical and pulse radiolysis observations have been rationalized in terms of the mechanism shown in Scheme 2, as follows. One-electron reduction of $[\mathbf{Co}]^{2+}$, followed by reaction with CO_2 and formate, leads to a mixture of $[\mathbf{Co}(CO_2)(HCO_2)]$ and $[(CO_2)\mathbf{Co}–OC(O)–\mathbf{Co}(HCO_2)]^+$. Further one-electron reduction of $[\mathbf{Co}(CO_2)(HCO_2)]$ by the $CO_2^{\bullet-}$ radical generated by pulse radiolysis, with a rate constant of 6.3×10^7 M^{-1} s^{-1}, corresponds to the faster component of the 1224 cm^{-1} bleach (Figures 4D and 4F, and eq. 7). The formation of four-coordinate $[\mathbf{Co}(CO_2)]$ is accompanied by the loss of bound formate, based on the calculations that predict this species to be more stable than $[\mathbf{Co}(CO_2)(HCO_2)]^-$ (Scheme 1). The relatively long-lived transient feature observed around 1200 cm^{-1} (Figure 4B) is most likely due to doubly-reduced $[\mathbf{Co}(CO_2)]$ since its decay rate (55 s^{-1} at 2 mM Co concentration) is similar to the slower growth rate of the $[\mathbf{Co}(CO)]^+$ product.

Scheme 2. Proposed mechanism of CO_2 reduction promoted by $[Co]^{2+}$ in dry CH_3CN in the presence of formate anion. Methyl groups and hydrogen atoms of the HMD ligand are omitted for clarity. PR

indicates the reduction steps initiated by pulse radiolysis, numbers in square brackets refer to equation numbers in the text.

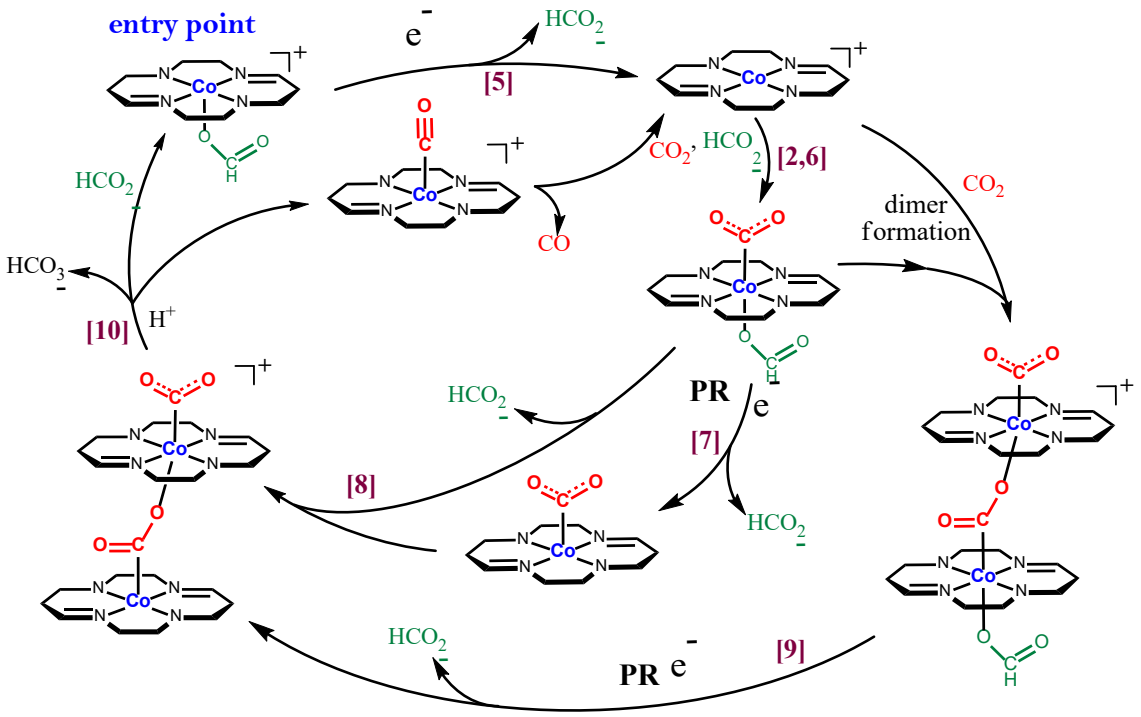

$$[\mathbf{Co}(CO_2)(HCO_2)] + CO_2^{\bullet-} \rightarrow [\mathbf{Co}(CO_2)] + CO_2 + HCO_2^- \quad k_7 = 6.3 \times 10^7\ M^{-1}\ s^{-1} \qquad (7)$$

$$[\mathbf{Co}(CO_2)] + [\mathbf{Co}(CO_2)(HCO_2)] \rightarrow [(CO_2)\mathbf{Co}\text{–}OC(O)\text{–}\mathbf{Co}]^+ + HCO_2^- \quad k_8 = 6.3 \times 10^7\ M^{-1}\ s^{-1} \qquad (8)$$

The slow component of the 1224 cm^{-1} bleach (Figures 4D and 4H), and the slow component of the bi-exponential growth of $[\mathbf{Co}(CO)]^+$ at 1917 cm^{-1} (Figures 4C and 4G), show a similar pseudo-first order dependence on $[\mathbf{Co}]^+$ concentration and are rationalized by the reaction of the doubly-reduced $[\mathbf{Co}(CO_2)]$ intermediate generated by pulse radiolysis with the singly-reduced $[\mathbf{Co}(CO_2)(HCO_2)]$ (eq. 8). The involvement of two Co complexes in the formation of $[\mathbf{Co}(CO)]^+$ under the conditions of the transient experiment is primarily dictated by the charge stoichiometry. Formation of the observed $[\mathbf{Co}(CO)]^+$ product requires the reduction of the singly-reduced $[\mathbf{Co}(CO_2)(HCO_2)]$ by an additional *two-electrons*. While all excess charge produced transiently (i.e., $CO_2^{\bullet-}$) is rapidly consumed to reduce a small fraction (<1%) of singly-reduced complexes

(eq. 7), the only available additional source of electrons is the singly-reduced complex itself. Thus, the first electron comes from pulse radiolysis (eq. 7) and the second is derived from a [**Co**(CO_2)(HCO_2)] molecule (eq. 8). Reduction by only a single electron would result in the formation of [**Co**(CO)]$^{2+}$. Dose-dependent pulse radiolysis measurements afforded different concentrations of [**Co**(CO_2)], which did not result in significantly different kinetics. This excludes the disproportionation of two [**Co**(CO_2)] species as a potential pathway for the formation of [**Co**(CO)]$^{+}$. The involvement of two [**Co**(CO_2)(HCO_2)] molecules in the formation of [**Co**(CO)]$^{+}$ is also supported by the observed consumption of two equivalents of the former species associated with the production of one equivalent of the latter in the PR-TRIR experiments (see Figures 4C and 4D and corresponding results section).

The reduction of the bimetallic intermediate, [(CO_2)**Co**–OC(O)–**Co**(HCO_2)]$^{+}$ by $CO_2^{\bullet-}$ (eq. 9) proceeds in parallel with the reduction of monometallic [**Co**(CO_2)(HCO_2)]. The rates of both reactions are probably similar as evidenced by the kinetics at 1224 cm^{-1} and their similar predicted reduction potentials (Scheme 1). However, a more accurate distinction is difficult due to strong spectral overlap of both species.

[(CO_2)**Co**–OC(O)–**Co**(HCO_2)]$^{+}$ + $CO_2^{\bullet-}$ → [(CO_2)**Co**–OC(O)–**Co**]$^{+}$ + CO_2 + HCO_2^{-} $k_9 \approx 6.3 \times 10^7$ M^{-1} s^{-1} (9)

[(CO_2)**Co**–OC(O)–**Co**]$^{+}$ + H^{+} + HCO_2^{-} → [**Co**(CO)]$^{+}$ + [**Co**(HCO_2)]$^{+}$ + HCO_3^{-} $k_{10} = 2.8 \times 10^4$ s^{-1} (10)

The faster component of the bi-exponential growth of [**Co**(CO)]$^{+}$ observed at 1917 cm^{-1} (Figures 4C and 4G) corresponds to the pathway originating from the reduced bimetallic species (eq. 10). This pathway does not require the diffusion of two Co complexes to form final product, which is consistent with the independence of its rate on the concentration of singly-reduced complex (Figure 4E), assuming that the rate of dimer reduction (eq. 9) is faster than the rate of formation of [**Co**(CO)]$^{+}$ (eq. 10). As the concentration of the Co complex increases, the amplitude of the fast component for the formation of [**Co**(CO)]$^{+}$ also increases (Fig. S3.2), indicating an increased concentration of the CO_2–bridged bimetallic complex prior to the electron pulse. Both mono- and bimetallic pathways transiently converge on a common intermediate, [(CO_2)**Co**–OC(O)–**Co**]$^{+}$, which further converts into [**Co**(CO)]$^{+}$, [**Co**(HCO_2)]$^{+}$, and bicarbonate, with the latter being identified as a co-product in IR-SEC experiments. Both the fast and slow components

of the [**Co**(CO)]$^+$ growth are independent of CO_2 concentration (Figure S3.3), which indicates that C–O bond cleavage through oxide transfer to an unbound CO_2 is an unlikely elementary step.

While our experimental data do not provide any further insight into the elementary steps for the conversion of the [**Co**(CO_2)]^0 and [(CO_2)**Co**–OC(O)–**Co**]$^+$ intermediates into the observed [**Co**(CO)]$^+$ and HCO_3^- products, theoretical calculations have been employed to probe these steps (Scheme 3). The experimental observation of bicarbonate anion clearly indicates that a proton source is present in the solution during catalysis. The involvement of residual water is unlikely considering the vigorous solvent and reagent drying methods and air-free sample preparation techniques employed (see Experimental section), especially considering the millisecond time scale for the formation of [**Co**(CO)]$^+$. On the other hand, decomposition of TBA^+ is known to provide protons together with the formation of *tert*-butyl amine and 1-butene (eq. 11).[38] The apparent pK_a value of TBA^+ in CH_3CN based on our calculations was predicted to be around 17 (eq. 11). A noticeable enhancement of CO evolution has been observed upon addition of 50 mM [TBA]$^+$[PF_6]$^-$ into the solution of [**Co**]$^{2+}$ during photocatalytic CO_2 reduction (Fig. S4.3). Also, *tert*-butyl amine has been detected by GC-MS after the photolysis experiment, confirming the role of TBA^+ as a proton source.

$$(C_4H_9)_4N^+ \rightleftharpoons (C_4H_9)_3N + C_4H_8 + H^+ \qquad pK_a^{app} = 17 \qquad (11)$$

While the direct protonation of the [**Co**(CO_2)]^0 and [(CO_2)**Co**–OC(O)–**Co**]$^+$ intermediates by TBA^+ is computed to be thermodynamically favorable (Figure S2.9), kinetically these reactions are not expected to occur to a significant extent. The protonation of [**Co**(CO_2)]^0 leads to an intermediate, [**Co**(CO_2H)]$^+$, which is almost 11 kcal/mol more stable compared to [(CO_2)**Co**–OC(O)–**Co**]$^+$, which forms by a competing pathway. Such a protonation would therefore prevent the formation of the bimetallic intermediate, [(CO_2)**Co**–OC(O)–**Co**]$^+$, which contradicts the experimental observation of the reaction between singly- and doubly-reduced Co complexes (Figures 4G and 4H, eq. 10). This discrepancy most likely arises from the existence of a substantial kinetic barrier for such a reaction, which would require significant structural changes and bond breaking in TBA^+ in addition to the release of a proton. The protonation of the bridged CO_2 in [(CO_2)**Co**–OC(O)–**Co**]$^+$ would be kinetically hindered for similar reasons, in addition to the significant steric hindrance near the bridging CO_2 molecule, slowing the proton transfer even further. Alternatively, we propose that a proton at one of the nitrogen atoms of an HMD ligand

(Scheme 1) acts as an internal proton relay within the bimetallic [(CO_2)**Co**–OC(O)–**Co**]$^+$ complex, leading to the formation of a bridged metallocarboxylic acid and a deprotonated HMD ligand ($\Delta G^{\ddagger}$ = 14.7 kcal/mol, ΔG = 14.1 kcal/mol), as shown in Scheme 3 and Figure 5. This proposed reactivity is supported by the absence of catalytic activity of a structurally similar N-methylated cyclam Co complex, which lacks ligand-based acid functionality.[20]

Scheme 3. Elementary steps for the transformation of the [Co(CO_2)]^0 and [(CO_2)Co–OC(O)–Co]$^+$ intermediates into [Co(CO)]$^+$ based on theoretical calculations. Computed free energy changes between intermediates and selected transition states at the M06-L level of theory are presented in units of kcal/mol.

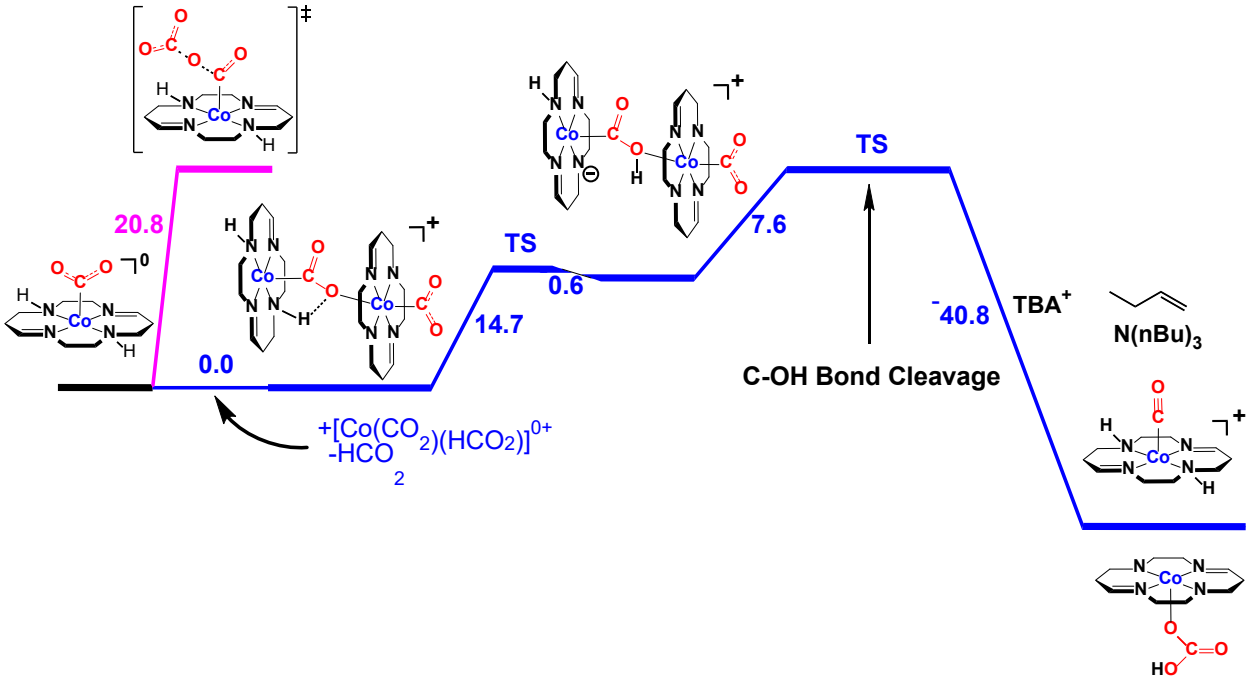

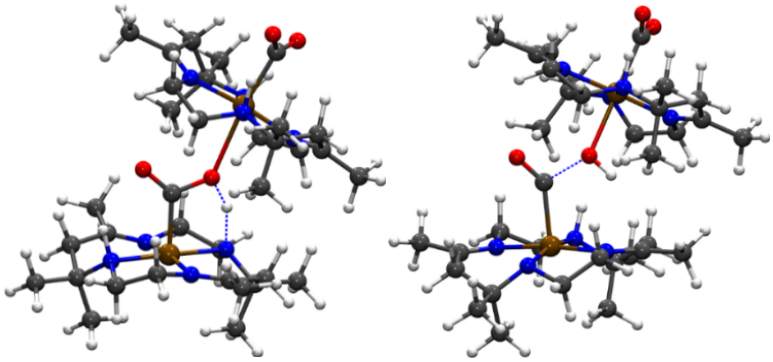

Figure 5. Optimized transition state structures at the M06-L level of theory for **(left)** internal proton transfer in $[(CO_2)\mathbf{Co}–OC(O)–\mathbf{Co}]^+$ and **(right)** C–OH bond cleavage in $[(CO_2)(HMD)Co(CO_2H)(HMD–H)]^+$. Color code: Co, ochre; C, gray; N, blue; O, red; H; white.

Protonation of the bridging CO_2 ligand promotes C–OH bond cleavage ($\Delta G^{\ddagger}$ = 7.6 kcal/mol), and subsequent protonation and isomerization steps generate the observed $[\mathbf{Co}(CO)]^+$ and cobalt (II) bicarbonate species (ΔG = –40.8 kcal/mol). While similar ligand-assisted protonation can be expected for the monometallic $[\mathbf{Co}(CO_2)]$ species, the barrier for this step appears to be less favorable compared to the bimetallic pathway (Fig. S2.9).

In summary, this work presents spectroscopic, kinetic and computational characterization of all major steps of a proposed catalytic cycle for CO_2 reduction mediated by the $[Co(HMD)]^{2+}$ catalyst in dry CH_3CN. One-electron reduction of the catalyst in the presence of CO_2 and formate anion leads to the formation of a mixture of monometallic and bimetallic forms of the CO_2 adduct, i.e., $[\mathbf{Co}(CO_2)(HCO_2)]$ and $[(CO_2)\mathbf{Co}–OC(O)–\mathbf{Co}(HCO_2)]^+$. A second reduction step produces a common bimetallic intermediate, $[(CO_2)\mathbf{Co}–OC(O)–\mathbf{Co}]^+$, either by direct reduction of $[(CO_2)\mathbf{Co}–OC(O)–\mathbf{Co}(HCO_2)]^+$ or by the reaction of doubly-reduced $[\mathbf{Co}(CO_2)]$ with singly-reduced $[\mathbf{Co}(CO_2)(HCO_2)]$. The conversion of the bridging CO_2 ligand to a bridging carboxylic acid, proceeds with the HMD ligand acting as an intermediary proton source, which results in facile cleavage of the C–OH bond within the bimetallic intermediate. This step is predicted to be rate limiting, since no kinetic dependence on CO_2 concentration was observed, in agreement with theoretical calculations. The overall evidence points to the bimetallic pathway enabling access to elementary steps with lower energy requirements and allowing utilization of the ligand as an internal proton source, resulting in overall catalysis being kinetically more facile as compared to

the monometallic pathway. The presence of a coordinating species, e.g., formate anion, appears to assist in the formation of the bimetallic intermediate. We propose that the bimetallic pathway allows the advancement of the catalyst through a series of highly reactive intermediates at a much higher rate as compared to the monometallic route, providing these unstable intermediates with less time to engage in deactivation side reactions. This in turn, will result in overall higher catalyst stability and increased product yields even at longer timescales of catalysis. This proposal is in accord with the improved photocatalytic performance of $[\mathbf{Co}(CO)]^{2+}$ by ca. 4.5× in the presence of formate anion at catalyst concentrations (such as [Co] = 4 mM) where the amount of bimetallic intermediate is expected to be significant.

This work opens up new opportunities for the development of more efficient CO_2 reduction catalysts that take advantage of lower energy bimetallic pathways, and pulse radiolysis with time-resolved IR detection is likely to play a key role in unraveling their mechanistic pathways.

Experimental Section

Materials. Acetonitrile (Aldrich, HPLC Plus) was distilled from potassium borohydride, dried over activated 3Å molecular sieves, and vacuum transferred into a vacuum-tight vessel to be used for sample preparations inside a glove box. *N-rac*-$[Co(HMD)(H_2O)](ClO_4)_2$ was prepared according to literature procedures.[33] $[TBA]^+[PF_6]^-$ (Fluka) was twice recrystallized from an ethanol/water mixture and dried under 10^{-6} torr vacuum. $[TBA]^+[HCO_2]^-$ was prepared according to a literature procedure.[30] All gases were research grade or higher except $^{13}CO_2$ that was 99.8% pure with 99% isotope enrichment (Cambridge Isotope Laboratories).

Electrochemistry and IR Spectroelectrochemistry (IR-SEC). All solutions for electrochemistry and IR-SEC were prepared inside a N_2 atmosphere glove box from dry solvents and solid materials. Solutions were saturated with CO_2 or $^{13}CO_2$ inside the glove box and transferred to the IR-SEC cell or electrochemical vessel using dry, gas-tight syringes (e.g., Hamilton 1002C). All cells for electrochemical measurements were thoroughly dried in a vacuum oven at 40 °C for at least 8 hours. Cyclic voltammetry was conducted using a BASi Epsilon potentiostat with a three-electrode configuration using Pt disk (working), Pt wire (auxiliary) and solid-state Ag/AgCl leakless (eDAQ, ET072) electrodes. Ferrocene was added to the solution at the end of the measurements to obtain

the reference potential. A custom reflective infrared spectroelectrochemical (IR-SEC) cell with boron-doped diamond working, platinum wire counter, and Ag/AgCl leakless (eDAQ, ET072) electrodes was used with a Fourier transform infrared spectrometer (Bruker, Vertex 80v) using a VeeMAX III Variable Angle Specular Reflectance Accessory (Pike Technologies), and the IR absorption changes were monitored following application of fixed potentials.

Sodium Amalgam Reduction. The chemical reduction of $[\mathbf{Co}]^{2+}$ was performed inside a N_2 atmosphere glove box using custom glassware by intermittently treating an acetonitrile solution of the metal complex with 0.5 % Na in Hg. The progression of the reduction was followed by monitoring changes in the UV-Vis spectra of $[\mathbf{Co}]^{2+}$ and $[\mathbf{Co}]^{+}$.

Pulse Radiolysis. Experiments were conducted using a custom-built flow mixing system, comprising of a four-way mixer (IDEX Health and Science) equipped with fluidic ¼-28 flat bottom connection ports attached to three gas-tight Hamilton syringes and to a custom-built, 1.93 mm pathlength, pulse radiolysis IR transmission flow cell[27] by means of stainless-steel tubing. All connections were completely air-tight and have been tested under vacuum. All the parts of the flow system were thoroughly dried in a vacuum oven for at least 8 hours and assembled inside a glove box. Three syringes were loaded with an acetonitrile solution of $[\mathbf{Co}]^{+}$, $[TBA]^{+}[H^{13}CO_2]^{-}$ in CO_2-saturated acetonitrile, and pure acetonitrile, respectively and connected to the flow system inside the glove box. The fully assembled flow setup was transferred from the glove box to the beamline of the LEAF electron accelerator.[28] The syringes were attached to three computer-controlled syringe pumps (New Era Pump Systems, NE-1000). Using custom LabView code to control the syringe pumps remotely, various concentrations of Co complex were produced while keeping the concentration of the other components constant. The time to deliver 0.2 mL aliquots for filling the IR cell was about 2 seconds. The TRIR measurements were performed in an identical manner as previously published,[27, 31] with the probe/reference IR beamsplitter ratio set to ca. 95/5. Tunable, continuous wave external-cavity quantum cascade lasers were used as the IR probe light (DRS Daylight Solutions, models 20152-MHF and 21084-MHF). The irradiated solution was replaced with freshly mixed solution by flowing a new 0.2 mL aliquot through the cell with the three syringe pumps. Only one kinetic trace per cell fill was measured.

Photolysis. Photocatalytic measurements have been conducted using a homebuilt setup described previously with some modifications.[41] A 150 W Xe lamp from PTI Instruments was used as a light

source and a Pyrex® glass vessel served as a UV filter (<300 nm). A mechanical shutter was automatically opened to irradiate solutions for pre-determined time intervals, the head space was analyzed for gaseous products after equilibration time of 6 minutes, and solutions were purged with CO_2 gas between each irradiation cycle.

Computational Methods.

Density functional theory. All geometries were fully optimized at the M06-L level of density functional theory[39] with the SMD continuum solvation model[40] for acetonitrile as solvent using the Stuttgart [8s7p6d2f | 6s5p3d1f] ECP10MDF contracted pseudopotential basis set[42] on Co and the 6-31G(d) basis set[43] on all other atoms. Non-analytical integrals were evaluated using the integral=grid=ultrafine option as implemented in the Gaussian 16 software package.[44] The nature of all stationary points was verified by analytic computation of vibrational frequencies, which were also used for the computation of zero-point vibrational energies, molecular partition functions, and for determining the reactants and products associated with each transition-state structure. Partition functions were used in the computation of 298 K thermal contributions to the free energy employing the usual ideal-gas, rigid-rotator, harmonic oscillator approximation.[45] Free-energy contributions were added to single-point, SMD-solvated M06-L electronic energies computed at the optimized geometries obtained with the initial basis with the SDD basis set on Co and the 6-311+G(2df,p) basis set on all other atoms to arrive at final, composite free energies.

Solvation and standard reduction potentials. As mentioned above, solvation effects for acetonitrile were accounted for by using the SMD continuum solvation model. A 1 M standard state was used for all species in solution. Thus, the free energy in solution is computed as the 1 atm gas-phase free energy, plus an adjustment for the 1 atm to 1 M standard-state concentration change of RT ln (24.5), or 1.9 kcal/mol, plus the 1 M to 1 M transfer (solvation) free energy computed from the SMD model.[45] The free energy of solvation of proton in acetonitrile is taken as –260.2 kcal/mol.[46]

Standard reduction potentials were calculated for various possible redox couples to assess the energetic accessibility of different intermediates at various oxidation states. For a redox reaction of the form

$$\boldsymbol{O}_{(soln)} \quad + \quad \boldsymbol{ne}^{-}_{(g)} \quad \rightarrow \quad \boldsymbol{R}_{(soln)} \qquad (1)$$

where *O* and *R* denote the oxidized and reduced states of the redox couple, respectively, and *n* is the number of electrons involved in redox reaction, the reduction potential $\boldsymbol{E^{o}_{O|R}}$ relative to SCE was computed as

$$\boldsymbol{E^{0}_{O|R}} = -\frac{\boldsymbol{\Delta G^{o}_{O|R}}}{\boldsymbol{nF}} - \boldsymbol{\Delta E^{o}_{ref}} \quad (2)$$

where $\boldsymbol{\Delta G^{o}_{O|R}}$ is the free energy change associated with eq. 1 (using Boltzmann statistics for the electron) and $\boldsymbol{\Delta E^{o}_{ref}}$ is taken as 0.141 V,[47] which is required for the conversion of calculated $\boldsymbol{E^{0}_{O|R}}$ versus normal hydrogen electrode (NHE) in aqueous solution (E_{NHE}= −4.281 V)[48] to $\boldsymbol{E^{0}_{O|R}}$ versus the saturated calomel electrode (SCE) in acetonitrile (E_{SCE} = −4.422 V).[49]

Supporting Information

Structures of geometric isomers of $[\mathbf{Co}]^{2+}$, CO_2 coordination geometries in $[\mathbf{Co}(CO_2)]^{+}$, IR-SEC results of $[\mathbf{Co}]^{2+}$ reduction with and without formate, pulse radiolysis of $[\mathbf{Co}(CO_2)(HCO_2)]$ and $[(CO_2)\mathbf{Co}–OC(O)–Co(HCO_2)]$, photocatalytic CO_2 reduction, energies and coordinates of optimized structures obtained from DFT calculations.

Acknowledgement

We thank Dr. Gerald Manbeck for his valuable comments. This work, and use of the LEAF facility of the BNL Accelerator Center for Energy Research, was carried out at Brookhaven National Laboratory and supported by the U.S. Department of Energy (DOE), Office of Science, Office of Basic Energy Sciences, Division of Chemical Sciences, Geosciences, & Biosciences, under contract DE-SC0012704. K.T.N. is grateful to the DOE for an Office of Science Graduate Student Research (SCGSR) award.

Present address:

[§]K.T.N.: U.S. Army Combat Capabilities Development Command Soldier Center, 15 General Greene Avenue, Natick, MA 01760, USA

References

1. Wang, J. W.; Zhong, D. C.; Lu, T. B., Artificial photosynthesis: Catalytic water oxidation and CO_2 reduction by dinuclear non-noble-metal molecular catalysts. *Coord. Chem. Rev.* **2018,** *377*, 225-236.
2. Cao, L. M.; Huang, H. H.; Wang, J. W.; Zhong, D. C.; Lu, T. B., The synergistic catalysis effect within a dinuclear nickel complex for efficient and selective electrocatalytic reduction of CO_2 to CO. *Green Chemistry* **2018,** *20*, 798-803.
3. Mohamed, E. A.; Zahran, Z. N.; Naruta, Y., Efficient electrocatalytic CO_2 reduction with a molecular cofacial iron porphyrin dimer. *Chem. Commun.* **2015,** *51*, 16900-16903.
4. Guo, Z. G.; Chen, G.; Cometto, C.; Ma, B.; Zhao, H. Y.; Groizard, T.; Chen, L. J.; Fan, H. B.; Man, W. L.; Yiu, S. M.; Lau, K. C.; Lau, T. C.; Robert, M., Selectivity control of CO versus HCOO- production in the visible-light-driven catalytic reduction of CO_2 with two cooperative metal sites. *Nature Catalysis* **2019,** *2*, 801-808.
5. Ouyang, T.; Wang, H. J.; Huang, H. H.; Wang, J. W.; Guo, S.; Liu, W. J.; Zhong, D. C.; Lu, T. B., Dinuclear metal synergistic catalysis boosts photochemical CO_2-to-CO conversion. *Angew. Chem. Int. Ed.* **2018,** *57*, 16480-16485.
6. Steffey, B. D.; Curtis, C. J.; DuBois, D. L., Electrochemical reduction of CO_2 catalyzed by a dinuclear palladium complex containing a bridging hexaphosphine ligand: evidence for cooperativity. *Organometallics* **1995,** *14*, 4937-4943.
7. Du, J. P.; Wilting, A.; Siewert, I., Are two metal ions better than one? Mono- and binuclear alpha-diimine-Re(CO)$_3$ complexes with proton-responsive ligands in CO_2 reduction catalysis. *Chem. Eur. J.* **2019,** *25*, 5555-5564.
8. Yang, W. W.; Roy, S. S.; Pitts, W. C.; Nelson, R. L.; Fronczek, F. R.; Jurss, J. W., Electrocatalytic CO_2 reduction with cis and trans conformers of a rigid dinuclear rhenium complex: comparing the monometallic and cooperative bimetallic pathways. *Inorg. Chem.* **2018,** *57*, 9564-9575.
9. Hayashi, Y.; Kita, S.; Brunschwig, B. S.; Fujita, E., Involvement of a binuclear species with the Re−C(O)O−Re moiety in CO_2 reduction catalyzed by tricarbonyl Rhenium(I) complexes with diimine ligands: strikingly slow formation of the Re−Re and Re−C(O)O−Re species from Re(dmb)(CO)$_3$S (dmb = 4,4'-dimethyl-2,2‘-bipyridine, S = solvent). *J. Am. Chem. Soc.* **2003,** *125*, 11976-11987.
10. Agarwal, J.; Fujita, E.; Schaefer, H. F.; Muckerman, J. T., Mechanisms for CO production from CO_2 using reduced Rhenium tricarbonyl catalysts. *J. Am. Chem. Soc.* **2012,** *134*, 5180-5186.
11. Rezaei, B.; Mokhtarianpour, M.; Ensafi, A. A.; Hadadzadeh, H.; Shakeni, J., Electrocatalytic reduction of CO_2 using the dinuclear Rhenium(I) complex ReCl(CO)$_3$(mu-tptzH)Re(CO)$_3$. *Polyhedron* **2015,** *101*, 160-164.
12. Wilting, A.; Stolper, T.; Mata, R. A.; Siewert, I., Dinuclear Rhenium complex with a proton responsive ligand as a redox catalyst for the electrochemical CO_2 reduction. *Inorg. Chem.* **2017,** *56*, 4176-4185.
13. Giereth, R.; Lang, P.; McQueen, E.; Meissner, X.; Braun-Cula, B.; Marchfelder, C.; Obermeier, M.; Schwalbe, M.; Tschierlei, S., Elucidation of cooperativity in CO_2 reduction using a xanthene-bridged bimetallic Rhenium(I) complex. *ACS Catal.* **2021,** *11*, 390-403.
14. Machan, C. W.; Chabolla, S. A.; Yin, J.; Gilson, M. K.; Tezcan, F. A.; Kubiak, C. P., Supramolecular assembly promotes the electrocatalytic reduction of carbon dioxide by Re(I) bipyridine catalysts at a lower overpotential. *J. Am. Chem. Soc.* **2014,** *136*, 14598-14607.

15. Paul, L. A.; Rajabi, S.; Jooss, C.; Meyer, F.; Ebrahimi, F.; Siewert, I., A dinuclear rhenium complex in the electrochemically driven homogeneous and heterogeneous H^+/CO_2 reduction. *Dalton Trans.* **2020,** *49*, 8367-8374.
16. Ouyang, T.; Huang, H. H.; Wang, J. W.; Zhong, D. C.; Lu, T. B., A dinuclear cobalt cryptate as a homogeneous photocatalyst for highly selective and efficient visible-light driven CO_2 reduction to CO in CH_3CN/H_2O solution. *Angew. Chem. Int. Ed.* **2017,** *56*, 738-743.
17. Realista, S.; Almeida, J. C.; Milheiro, S. A.; Bandeira, N. A. G.; Alves, L. G.; Madeira, F.; Calhorda, M. J.; Martinho, P. N., Co-II cryptates convert CO_2 into CO and CH_4 under visible light. *Chem. Eur. J.* **2019,** *25*, 11670-11679.
18. Fisher, B.; Eisenberg, R., Electrocatalytic reduction of carbon dioxide by using macrocycles of Nickel and Cobalt. *J. Am. Chem. Soc.* **1980,** *102*, 7361-7363.
19. Tinnemans, A. H. A.; Koster, T. P. M.; Thewissen, D.; Mackor, A., Tetraaza-macrocyclic Cobalt(II) and Nickel(II) complexes as electron-transfer agents in the photoelectrochemical and electrochemical reduction of carbon dioxide. *Recl. Trav. Chim. Pays-Bas* **1984,** *103*, 288-295.
20. Matsuoka, S.; Yamamoto, K.; Ogata, T.; Kusaba, M.; Nakashima, N.; Fujita, E.; Yanagida, S., Efficient and selective electron mediation of Cobalt complexes with cyclam and related macrocycles in the *p*-terphenyl-catalyzed photoreduction of CO_2. *J. Am. Chem. Soc.* **1993,** *115*, 601-609.
21. Creutz, C.; Chou, M. H., Hydricities of d^6 metal hydride complexes in water. *J. Am. Chem. Soc.* **2009,** *131*, 2794-2795.
22. Pitman, C. L.; Brereton, K. R.; Miller, A. J. M., Aqueous Hydricity of Late Metal Catalysts as a Continuum Tuned by Ligands and the Medium. *J. Am. Chem. Soc.* **2016,** *138*, 2252-2260.
23. Brereton, K. R.; Jadrich, C. N.; Stratakes, B. M.; Miller, A. J. M., Thermodynamic Hydricity across Solvents: Subtle Electronic Effects and Striking Ligation Effects in Iridium Hydrides. *Organometallics* **2019,** *38*, 3104-3110.
24. Mathis, C. L.; Geary, J.; Ardon, Y.; Reese, M. S.; Philliber, M. A.; VanderLinden, R. T.; Saouma, C. T., Thermodynamic Analysis of Metal–Ligand Cooperativity of PNP Ru Complexes: Implications for CO2 Hydrogenation to Methanol and Catalyst Inhibition. *J. Am. Chem. Soc.* **2019,** *141*, 14317-14328.
25. Fujita, E.; Szalda, D. J.; Creutz, C.; Sutin, N., Carbon dioxide activation: Thermodynamics of CO_2 binding and the involvement of two cobalt centers in the reduction of CO_2 by a cobalt(I) macrocycle. *J. Am. Chem. Soc.* **1988,** *110*, 4870-4871.
26. Fujita, E.; Szalda, D. J., Crystallization and structure of a binuclear species containing the Co-C(OH)-O-Co moiety. *Inorg. Chim. Acta* **2000,** *297*, 139-144.
27. Grills, D. C.; Farrington, J. A.; Layne, B. H.; Preses, J. M.; Bernstein, H. J.; Wishart, J. F., Development of nanosecond time-resolved infrared detection at the LEAF pulse radiolysis facility. *Rev. Sci. Instrum.* **2015,** *86*, 044102.
28. Wishart, J. F.; Cook, A. R.; Miller, J. R., The LEAF picosecond pulse radiolysis facility at Brookhaven National Laboratory. *Rev. Sci. Instrum.* **2004,** *75*, 4359-4366.
29. Grills, D. C.; Polyansky, D. E.; Fujita, E., Application of pulse radiolysis to mechanistic investigations of catalysis relevant to artificial photosynthesis. *ChemSusChem* **2017,** *10*, 4359 – 4373.
30. Grills, D. C.; Lymar, S. V., Radiolytic formation of the carbon dioxide radical anion in acetonitrile revealed by transient IR spectroscopy. *Phys. Chem. Chem. Phys.* **2018,** *20*, 10011-10017.
31. Grills, D. C.; Farrington, J. A.; Layne, B. H.; Lymar, S. V.; Mello, B. A.; Preses, J. M.; Wishart, J. F., Mechanism of the formation of a Mn-based CO_2 reduction catalyst revealed by pulse radiolysis with time-resolved infrared detection. *J. Am. Chem. Soc.* **2014,** *136*, 5563-5566.
32. Fujita, E.; Creutz, C.; Sutin, N.; Szalda, D. J., Carbon dioxide activation by Cobalt(I) macrocycles: Factors affecting CO_2 and Co binding. *J. Am. Chem. Soc.* **1991,** *113*, 343-353.
33. Szalda, D. J.; Schwarz, C. L.; Endicott, J. F.; Fujita, E.; Creutz, C., Solution studies of the Cobalt(II) *N-rac*-CoL^{2+} and *N-meso*-CoL^{2+} isomers and molecular and crystal structures of the low-spin, 5-coordinate Cobalt(II) macrocyclic complexes *N-rac*-$CoL(H_2O)(ClO_4)_2$ (1) and *N-rac*-$CoL(OClO_3)ClO_4$ (2) (L = 5,7,7,12,14,14-hexamethyl-1,4,8,11-tetraazacyclotetradeca-4,11-diene). *Inorg. Chem.* **1989,** *28*, 3214-3219.

34. Fujita, E.; Creutz, C.; Sutin, N.; Brunschwig, B. S., Carbon dioxide activation by cobalt macrocycles - evidence of hydrogen-bonding between bound CO_2 and the macrocycle in solution. *Inorg. Chem.* **1993,** *32*, 2657-2662.
35. Fujita, E.; Brunschwig, B. S.; Ogata, T.; Yanagida, S., Toward photochemical carbon dioxide activation by transition-metal complexes. *Coord. Chem. Rev.* **1994,** *132*, 195-200.
36. Morris, A. J.; Meyer, G. J.; Fujita, E., Molecular approaches to the photocatalytic reduction of carbon dioxide for solar fuels. *Acc. Chem. Res.* **2009,** *42*, 1983-1994.
37. Schneider, J.; Jia, H. F.; Muckerman, J. T.; Fujita, E., Thermodynamics and kinetics of CO_2, CO, and H^+ binding to the metal centre of CO_2 reduction catalysts. *Chem. Soc. Rev.* **2012,** *41*, 2036-2051.
38. Bolinger, C. M.; Story, N.; Sullivan, B. P.; Meyer, T. J., Electrocatalytic reduction of carbon dioxide by 2,2'-bipyridine complexes of Rhodium and Iridium. *Inorg. Chem.* **1988,** *27*, 4582-4587.
39. Zhao, Y.; Truhlar, D. G., A new local density functional for main-group thermochemistry, transition metal bonding, thermochemical kinetics, and noncovalent interactions. *J. Chem. Phys.* **2006,** *125*, 194101.
40. Marenich, A. V.; Cramer, C. J.; Truhlar, D. G., Universal solvation model based on solute electron density and on a continuum model of the solvent defined by the bulk dielectric constant and atomic surface tensions. *J. Phys. Chem. B* **2009,** *113*, 6378-6396.
41. Rotundo, L.; Grills, D. C.; Gobetto, R.; Priola, E.; Nervi, C.; Polyansky, D. E.; Fujita, E., Photochemical CO_2 Reduction Using Rhenium(I) Tricarbonyl Complexes with Bipyridyl-Type Ligands with and without Second Coordination Sphere Effects. *ChemPhotoChem* **2021,** *5*, 494-494.
42. Dolg, M.; Wedig, U.; Stoll, H.; Preuss, H., Energy-adjusted ab initio pseudopotentials for the first row transition elements. *J. Chem. Phys.* **1987,** *86*, 866-872.
43. Hehre, W. J. R., Leo; Schleyer, Paul von R.; Pople, John A., *Ab initio molecular orbital theory*. Wiley: New York, 1986.
44. Frisch, M. J. T., G. W.; Schlegel, H. B.; Scuseria, G. E.; Robb, M. A.; Cheeseman, J. R.; Scalmani, G.; Barone, V.; Petersson, G. A.; Nakatsuji, H.; Li, X.; Caricato, M.; Marenich, A. V.; Bloino, J.; Janesko, B. G.; Gomperts, R.; Mennucci, B.; Hratchian, H. P.; Ortiz, J. V.; Izmaylov, A. F.; Sonnenberg, J. L.; Williams-Young, D.; Ding, F.; Lipparini, F.; Egidi, F.; Goings, J.; Peng, B.; Petrone, A.; Henderson, T.; Ranasinghe, D.; Zakrzewski, V. G.; Gao, J.; Rega, N.; Zheng, G.; Liang, W.; Hada, M.; Ehara, M.; Toyota, K.; Fukuda, R.; Hasegawa, J.; Ishida, M.; Nakajima, T.; Honda, Y.; Kitao, O.; Nakai, H.; Vreven, T.; Throssell, K.; Montgomery, J. A., Jr.; Peralta, J. E.; Ogliaro, F.; Bearpark, M. J.; Heyd, J. J.; Brothers, E. N.; Kudin, K. N.; Staroverov, V. N.; Keith, T. A.; Kobayashi, R.; Normand, J.; Raghavachari, K.; Rendell, A. P.; Burant, J. C.; Iyengar, S. S.; Tomasi, J.; Cossi, M.; Millam, J. M.; Klene, M.; Adamo, C.; Cammi, R.; Ochterski, J. W.; Martin, R. L.; Morokuma, K.; Farkas, O.; Foresman, J. B.; Fox, D. J. *Gaussian 16*, Gaussian, Inc.: Wallingford CT, 2016.
45. Cramer, C. J., *Essentials of computational chemistry: theories and models*. 2nd Edition ed.; John Wiley & Sons Ltd: Chichester, 2004.
46. Kelly, C. P.; Cramer, C. J.; Truhlar, D. G., Single-ion solvation free energies and the normal hydrogen electrode potential in methanol, acetonitrile, and dimethyl sulfoxide. *J. Phys. Chem. B* **2007,** *111*, 408-422.
47. Keith, J. A.; Grice, K. A.; Kubiak, C. P.; Carter, E. A., Elucidation of the selectivity of proton-dependent electrocatalytic CO_2 reduction by *fac*-Re(bpy)$(CO)_3$Cl. *J. Am. Chem. Soc.* **2013,** *135*, 15823-15829.
48. Kelly, C. P.; Cramer, C. J.; Truhlar, D. G., Aqueous solvation free energies of ions and ion-water clusters based on an accurate value for the absolute aqueous solvation free energy of the proton. *J. Phys. Chem. B* **2006,** *110*, 16066-16081.
49. Isse, A. A.; Gennaro, A., Absolute potential of the standard hydrogen electrode and the problem of interconversion of potentials in different solvents. *J. Phys. Chem. B* **2010,** *114*, 7894-7899.

TOC graphic

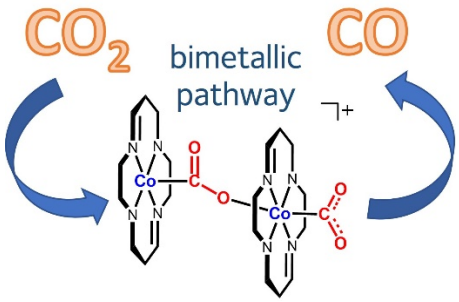

Supporting Information for:

The Role of Bimetallic Interactions in Enhancement of Catalytic CO_2 Reduction by a Macrocyclic Cobalt Catalyst

Dmitry E. Polyansky,*[a] David C. Grills,[a] Mehmed Z. Ertem,[a] Ken T. Ngo[b,c] and Etsuko Fujita[a]

[a] Chemistry Division, Brookhaven National Laboratory, Upton, New York 11973-5000, U.S.A.

[b] Department of Chemistry, University of Massachusetts Boston, 100 Morrissey Boulevard, Boston, MA 02125, USA

[c] Present address: U.S. Army Combat Capabilities Development Command Soldier Center, 15 General Greene Avenue, Natick, MA 01760, USA

*Email: dep@bnl.gov

Table of Contents

Section S0. Introduction.

Chart S0.1. The geometric isomers of $[Co]^{2+}$: *N-rac* isomer at left and *N-meso* isomer at right

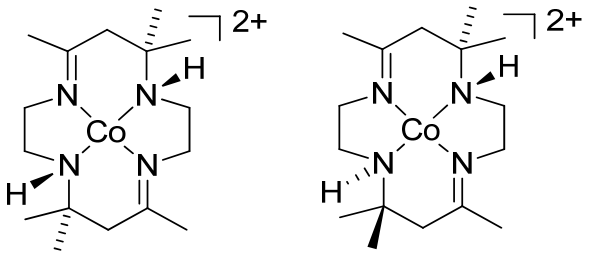

The coordination of the HMD ligand to a metal center results in two diastereomers, the *N-rac* and *N-meso* species (see Chart S0.1), with the *N-rac* isomer being the dominant (>> 90%) species in CH_3CN.[1] While the interconversion between *N*-meso and *N*-rac-$[\mathbf{Co}]^{2+}$ isomers is slow in neutral aqueous solutions ($< 2 \times 10^{-7}$ s^{-1}) or organic solvent, the conversion of $[\mathbf{Co}]^{+}$ is faster.[2] While *N*-meso-$[\mathbf{Co}]^{2+}$ with axial chloride ligands[3] and *N*-rac-$[\mathbf{Co}]^{2+}$ with axial water[1] are six- and five-coordinate, respectively, in the solid state as reported by their X-ray crystal structures, their coordination in solution is not well defined.[1, 3] The one-electron reduced $[\mathbf{Co}]^{+}$ species are primarily square planar as evidenced by their X-ray crystal structures, the weak solvent dependence of their UV-vis spectra[4] and from XAS experiments.[5]

Chart S0.2. CO_2 coordination geometries in $[Co(CO_2)]^{+}$ differing by the internal hydrogen bonding between the coordinated CO_2 and amine hydrogens of the macrocycle, and the presence or absence of a bound solvent molecule.[6] Reproduced from: Fujita, E.; Creutz, C.; Sutin, N.; Brunschwig, B. S., *Inorg. Chem.* 1993, *32*, 2657-2662. Copyright 1993 American Chemical Society.

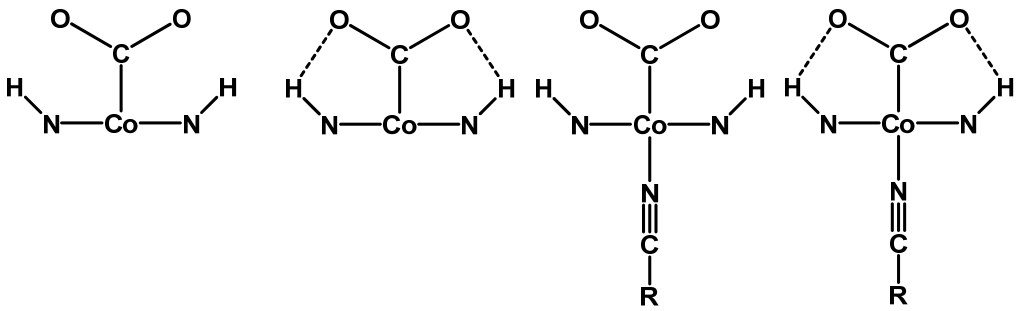

A solution of the CO_2 adduct in butyronitrile shows a reversible thermochromism: pale purple at room temperature and yellow below 160 K. The solid isolated at low temperature indicates that a solvent molecule coordinates at the sixth coordination site at low temperature (eq. 3, main text). Variable temperature IR spectroscopy was used to identify four forms of the $[\mathbf{Co}(CO_2)]^{+}$ adduct, differing by the internal hydrogen bonding between the coordinated CO_2 and the amine hydrogens

of the macrocycle, and the presence or absence of a bound solvent molecule: a five-coordinate, non-hydrogen bonded form, $[\mathbf{Co}(CO_2)]^+$ (ν_{CO} = 1710 cm^{-1}, ν_{NH} = 3208 cm^{-1}), a five-coordinate, intramolecularly hydrogen-bonded form, $[\mathbf{Co}(^{HB}CO_2)]^+$ (ν_{CO} = 1626 cm^{-1}), a six-coordinate, non-hydrogen bonded form, $[(S)\mathbf{Co}(CO_2)]^+$ (ν_{CO} = 1609 cm^{-1}, ν_{NH} = 3224 cm^{-1}), and a six-coordinate, hydrogen-bonded form, $[(S)\mathbf{Co}(^{HB}CO_2)]^+$ (ν_{CO} = 1544 cm^{-1}, ν_{NH} = 3145 cm^{-1}) (Chart S0.2).[6]

Scheme S0.1. The formation of solvent-derived radicals by pulse radiolysis of CH_3CN (top) and the reactions that occur in CO_2-saturated CH_3CN in the presence of HCO_2^-, leading to the one-electron reduction of a dissolved catalyst by $CO_2^{\bullet-}$ (bottom)

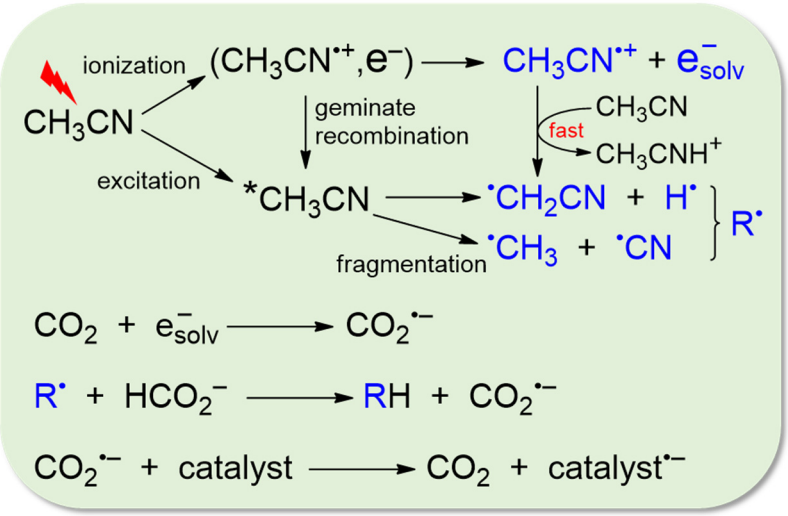

Section S1. Reduction of $[Co(HMD)]^{2+}$ in acetonitrile in the absence of formate.

Spectroelectrochemical infrared (IR-SEC) studies of $[\mathbf{Co}]^{2+}$ (where **Co** is the Co(HMD) molecule) have been conducted by applying a constant bias to the working electrode and acquiring IR spectra during the course of electrolysis. In dry CD_3CN under a N_2 atmosphere at an applied potential about 200 mV cathodic of the $Co^{II/I}$ potential (E_p = –1.83 V vs. Fc^+/Fc), IR spectral changes are consistent with the formation of $[\mathbf{Co}]^+$ (Fig. S1.1). Under a CO_2 atmosphere at an applied potential 100 mV anodic of the $Co^{II/I}$ potential (E_p = –1.74 V vs. Fc^+/Fc under CO_2), the formation of a five-coordinate $[\mathbf{Co}(CO_2)]^+$ species was observed (Fig. S1.2). Applying a potential 100 mV more negative of E_p results in the conversion of $[\mathbf{Co}(CO_2)]^+$ to $[\mathbf{Co}(CO)]^+$ and the formation of HCO_3^- (Fig. S1.3).

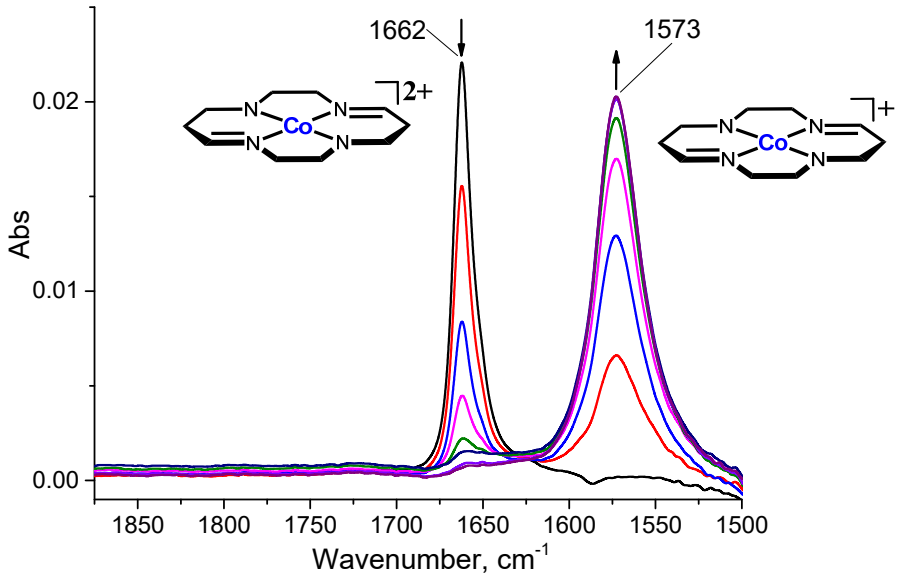

Figure S1.1. IR spectra measured during the electrochemical reduction of a 2 mM solution of $[\mathbf{Co}]^{2+}$ (the full structure is shown in Chart 1 in the main text) in dry CD_3CN containing 0.1 M $[TBA]^+[PF_6]^-$ under a N_2 atmosphere, at an applied potential of –2.0 V vs. Fc^+/Fc. Bands at 1662 cm^{-1} and 1573 cm^{-1} are the $\nu_{C=N}$ vibrational frequencies of the $[\mathbf{Co}]^{2+}$ and $[\mathbf{Co}]^+$ complexes, respectively.[7]

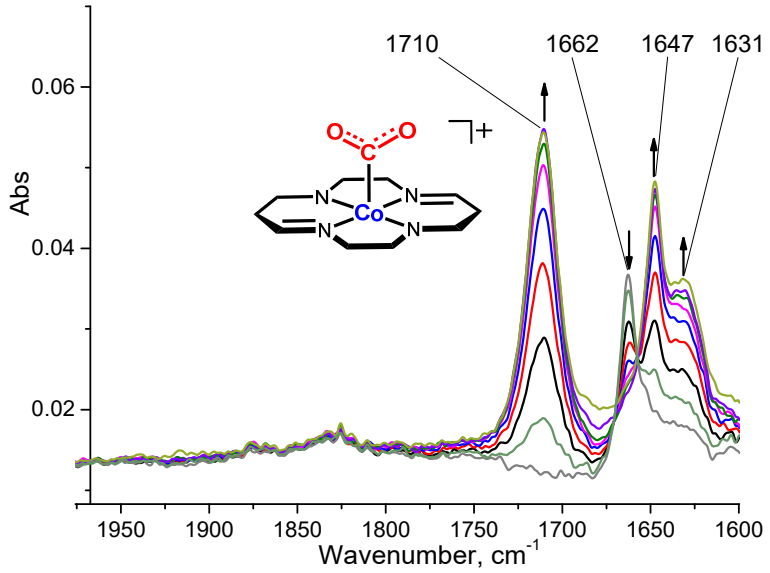

Figure S1.2. IR spectra measured during the electrochemical reduction of a 2 mM solution of [**Co**]$^{2+}$ in dry CD_3CN containing 0.1 M $[TBA]^+[PF_6]^-$ under a CO_2 atmosphere, at an applied potential of –1.64 V vs. Fc^+/Fc. Vibrations at $\nu_{C=O}$ = 1710 cm^{-1}, $\nu_{C=O}$ = 1631 cm^{-1}, and $\nu_{C=N}$ = 1647 cm^{-1} are due to the [**Co**$(CO_2)]^+$ complex.[7]

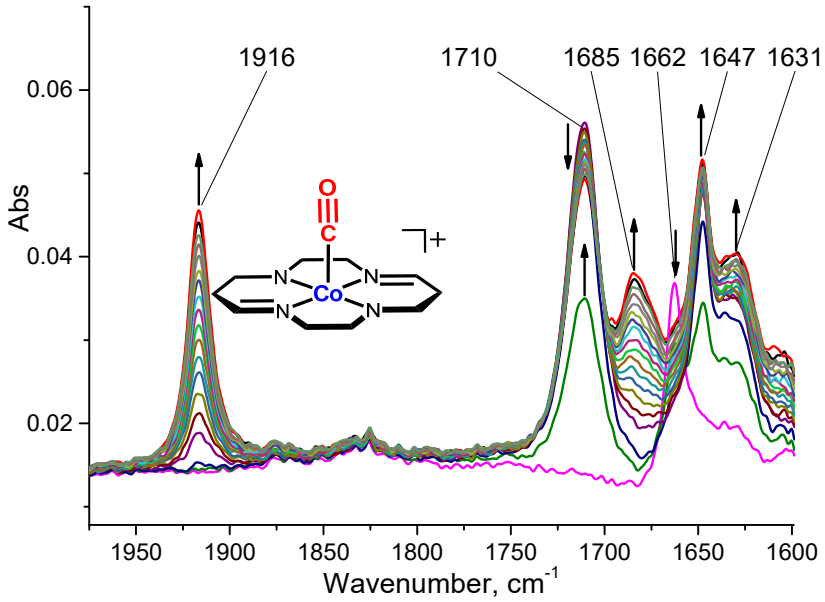

Figure S1.3. IR spectra measured during the electrochemical reduction of a 2 mM solution of [**Co**]$^{2+}$ in dry CD_3CN containing 0.1 M $[TBA]^+[PF_6]^-$ under a CO_2 atmosphere, at an applied potential of –1.84 V vs. Fc^+/Fc. The $\nu_{C=O}$ = 1916 cm^{-1} band is due to [**Co**$(CO)]^+$, and the $\nu_{C=O}$ = 1685 cm^{-1} band is assigned to HCO_3^-.[8]

Section S2. Reduction of $[Co(HMD)]^{2+}$ in acetonitrile in the presence of formate.

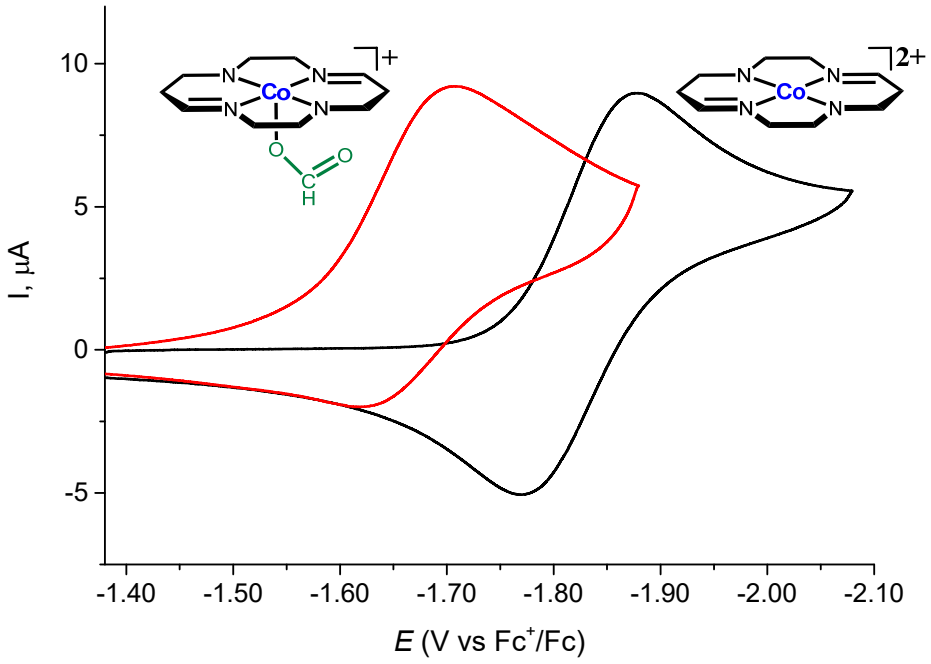

Figure S2.1. CVs of 2 mM [**Co**]$^{2+}$ in dry CH_3CN containing 0.1 M $[TBA]^+[PF_6]^-$under a N_2 atmosphere: without (black) and with (red) 50 mM $[TBA]^+[HCO_2]^-$. The forward scan peak shift is about 170 mV.

The IR spectrum of $[TBA]^+[H^{13}CO_2]^-$ in dry CD_3CN under a N_2 atmosphere exhibits a strong absorption around 1560 cm^{-1} associated with its antisymmetric carboxyl C=O stretch. The use of ^{13}C-labeled formate red-shifts the carboxyl C=O stretch ($\nu_{C=O}$ = 1607 cm^{-1} in $H^{12}CO_2^-$), opening the spectroscopic window around 1600 cm^{-1} for observation of the species of interest. Saturation of a $[TBA]^+[H^{13}CO_2]^-$ solution with CO_2 leads to a small decrease in the 1560 cm^{-1} peak and the appearance of a new band around 1683 cm^{-1}, which is attributed to the formation of a CO_2–$H^{13}CO_2^-$ adduct (Fig. S2.2).

The spectrum of [**Co**]$^{2+}$ in dry CD_3CN in the presence of $[TBA]^+[H^{13}CO_2]^-$ demonstrates the binding of formate to the Co center, forming five-coordinate [**Co**$(H^{13}CO_2)]^+$, as indicated by the consumption of free formate (1561 cm^{-1}) and the appearance of a new vibration at 1542 cm^{-1}, which is assigned to the C=O vibration of the bound ^{13}C-labeled formate anion (Fig. S2.3). It should be noted that in cases where the absorption maxima of the consumed and newly formed

species are close, which results in a derivative shape of the measured difference spectra (e.g., as shown in Fig. S2.3), the observed peak positions may not precisely correspond to the actual peak maxima due to spectral overlap. This may result in small deviations in peak maxima reported throughout this work.

The addition of CO_2 to a solution of $[\mathbf{Co}]^{2+}$ in dry CD_3CN in the presence of $[TBA]^+[H^{13}CO_2]^-$ has no effect on the spectrum of $[\mathbf{Co}(H^{13}CO_2)]^+$, indicating no interaction of CO_2 with this metal complex (Fig. S2.3). Interestingly, the 1683 cm^{-1} peak assigned to the CO_2–$H^{13}CO_2^-$ adduct red shifts to 1638 cm^{-1} upon addition of $^{13}CO_2$, consistent with the formation of the $^{13}CO_2$–$H^{13}CO_2^-$ adduct.

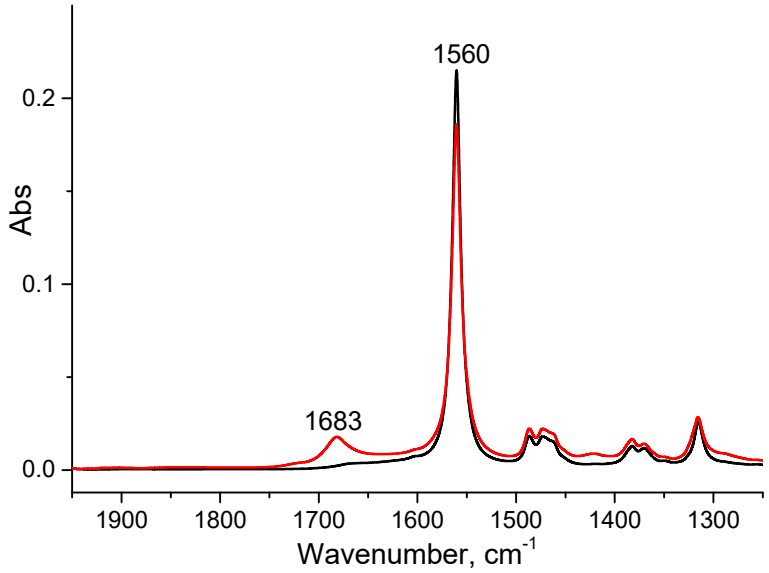

Figure S2.2. IR spectra of 12 mM $[TBA]^+[H^{13}CO_2]^-$ in CD_3CN measured in the absence (black) and presence (red) of CO_2. The $\nu_{C=O}$ = 1560 cm^{-1} band is due to free $H^{13}CO_2^-$ and the 1683 cm^{-1} peak is assigned to a CO_2–$H^{13}CO_2^-$ adduct.

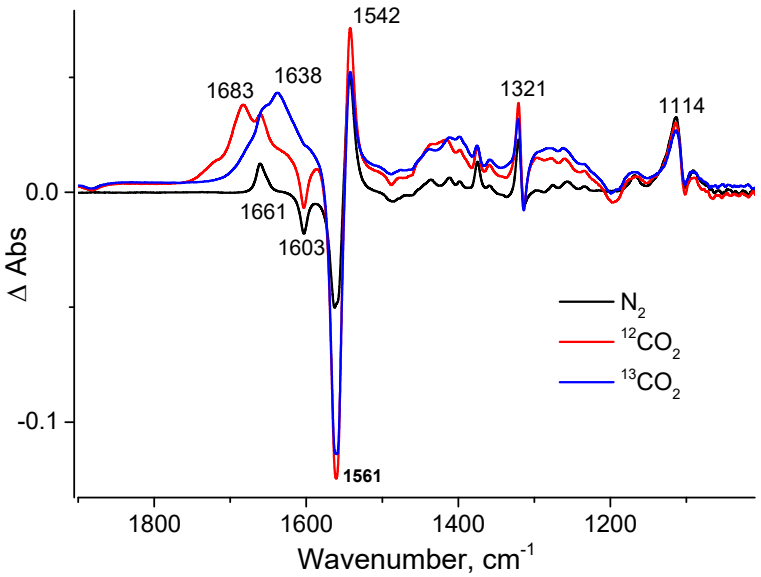

Figure S2.3. IR difference spectra of [**Co**]$^{2+}$ in dry CD_3CN in the presence of 20 mM $[TBA]^+[H^{13}CO_2]^-$ under N_2 (black), $^{12}CO_2$ (red), and $^{13}CO_2$ (blue) atmospheres. The baseline was taken with $[TBA]^+[H^{13}CO_2]^-$ present. Negative signals at 1603 cm^{-1} and 1561 cm^{-1} are due to the consumption of free formate, while the band at 1542 cm^{-1} is due to the bound ^{13}C-labeled formate in [**Co**$(H^{13}CO_2)]^+$. Bands at 1683 cm^{-1} and 1638 cm^{-1} are due to the $^{12}CO_2$–$H^{13}CO_2^-$ and $^{13}CO_2$–$H^{13}CO_2^-$ adducts, respectively (see Fig. S2.2). Signals at 1661 cm^{-1}, 1321 cm^{-1}, and 1114 cm^{-1} are due to the HMD macrocycle in [**Co**$(H^{13}CO_2)]^+$.

The reduction of [**Co**]$^{2+}$ in CD_3CN in the presence of $[TBA]^+[H^{13}CO_2]^-$ under a CO_2 atmosphere at an applied potential of –1.64 V vs. Fc^+/Fc, results in the formation of [**Co**$(CO_2)]^+$, which absorbs at 1710 cm^{-1}, and a new species absorbing around 1600 cm^{-1} (Fig. S2.4). As the concentration of formate is increased from 5 mM to 50 mM, the ratio of the peak intensities (1710 cm^{-1}/1600 cm^{-1}) decreases, with the 1710 cm^{-1} signal diminishing completely at the highest concentration of formate (Fig. S2.4, green). The signal at 1600 cm^{-1} is assigned to the antisymmetric $\nu_{C=O}$ stretch of bound CO_2 in the six-coordinate [**Co**$(CO_2)(H^{13}CO_2)$] complex. This assignment was confirmed by repeating the reduction in the presence of $^{13}CO_2$, where the new band red-shifted to ca. 1585 cm^{-1}, consistent with the formation of [**Co**$(^{13}CO_2)(H^{13}CO_2)$] (Fig. 2D, main text). In addition to the isotopic shift of the antisymmetric stretching vibration at 1600 cm^{-1}, the symmetric stretching mode of bound CO_2, observed around 1224 cm^{-1}, red-shifts to 1210 cm^{-1} upon ^{13}C labeling of the CO_2 ligand. Since the [**Co**$(CO_2)]^+$ and [**Co**$(CO_2)(H^{13}CO_2)$] complexes have non-overlapping absorbances at 1710 cm^{-1} and 1600 cm^{-1} respectively, equilibrium concentrations of both species can be accurately estimated from absorbance values at the corresponding peaks, assuming total

conversion of the starting [**Co**]$^{2+}$. For example, using the absorbance at 1710 cm^{-1}, the equilibrium concentration of [**Co**(CO$_2$)]$^+$ can be found as:

$$C(x\ mM\ added\ formate) = \frac{Abs(x\ mM\ added\ formate)}{Abs\ (0\ mM\ formate)} \times C(starting\ complex)$$

The equilibrium concentrations of other species can be found from the difference between the initial concentration of [**Co**]$^{2+}$ and the calculated concentration of one of the forms of reduced Co catalyst.

A plot of the ratio of *equilibrium* concentrations of [**Co**(CO$_2$)(H^{13}CO$_2$)] / [**Co**(CO$_2$)]$^+$ as a function of the *equilibrium* concentration of [TBA]$^+$[H^{13}CO$_2$]$^-$ (Fig. S2.5) can be used to determine the equilibrium constant for formate binding to [**Co**(CO$_2$)]$^+$ (eq. 6, main text), K_6 = 325 ± 7 M^{-1}.

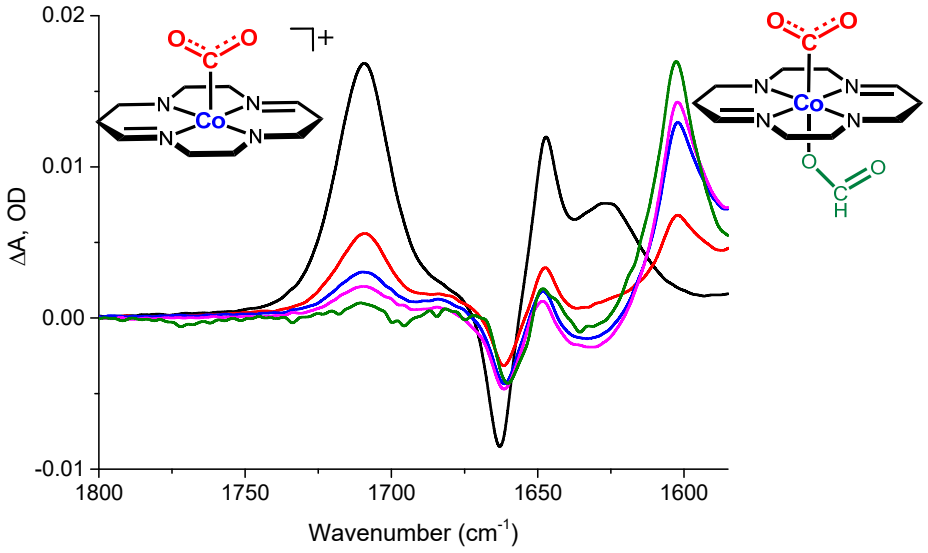

Fig. S2.4. IR difference spectra measured during electrochemical reduction of 2 mM solutions of [**Co**]$^{2+}$ in dry CD$_3$CN containing 0.1 M [TBA]$^+$[PF$_6$]$^-$ under a CO$_2$ atmosphere at an applied potential of –1.64 V vs. Fc$^+$/Fc: in the presence of 0 mM [TBA]$^+$[H^{13}CO$_2$]$^-$ (black); 5 mM [TBA]$^+$[H^{13}CO$_2$]$^-$ (red); 17 mM [TBA]$^+$[H^{13}CO$_2$]$^-$ (blue); 25 mM [TBA]$^+$[H^{13}CO$_2$]$^-$ (magenta); 50 mM [TBA]$^+$[H^{13}CO$_2$]$^-$ (green). The baseline was taken in the presence of [**Co**]$^{2+}$, 0.1 M [TBA]$^+$[PF$_6$]$^-$, [TBA]$^+$[H^{13}CO$_2$]$^-$, and CO$_2$.

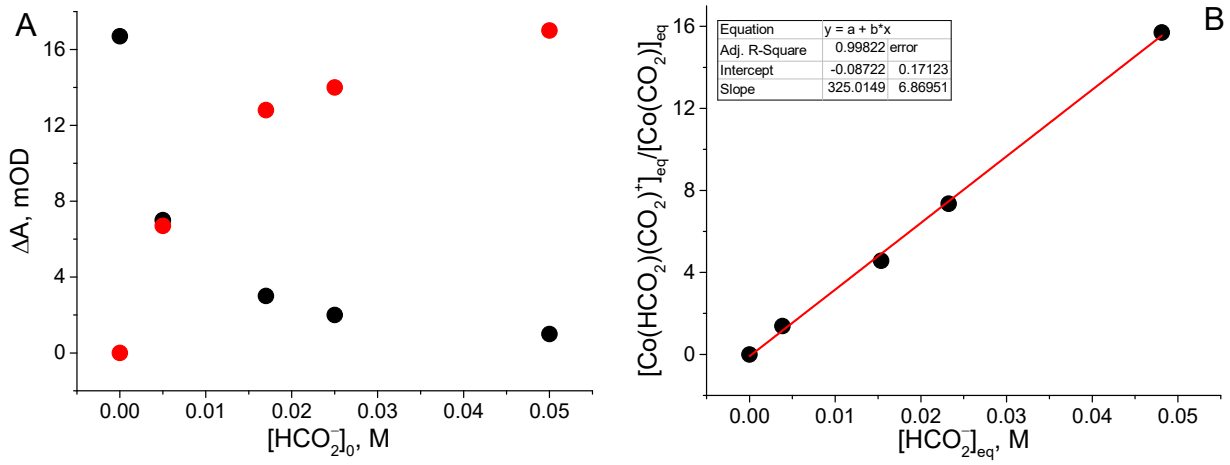

Fig. S2.5. Panel A: IR absorbance change at 1710 cm^{-1} (black) and 1600 cm^{-1} (red) as a function of added $[TBA]^+[H^{13}CO_2]^-$ based on the data in Fig. S2.3 Panel B: the ratio of *equilibrium* concentrations of $[\mathbf{Co}(CO_2)(H^{13}CO_2)]$ / $[\mathbf{Co}(CO_2)]^+$ as a function of *equilibrium* concentration of $[TBA]^+[H^{13}CO_2]^-$. The slope of the linear fit corresponds to $K_6 = 325 \pm 7\ M^{-1}$.

The calculated IR spectra of two isomers of $[\mathbf{Co}(CO_2)(H^{13}CO_2)]$ are shown in Fig. S2.6. One of the isomers contains a Co-bound CO_2 in which the O atoms are hydrogen-bonded to the HMD ligand through its HN groups (Fig. S2.6 A), while the other isomer features a hydrogen-bonded formate ion (Fig. S2.6 B). While the free energy of both species is almost identical within the computational precision, the IR spectrum of the CO_2 hydrogen-bonded isomer appears to match more closely to the experimental spectrum in Fig. 2 (main text). Following the crystallographic identification of a CO_2-bridged dimer of the singly-reduced complex,[9] several stable CO_2-bridged dimer species containing formate ion have been identified computationally. One form of the dimer contains a formate ion as the sixth ligand at both Co centers, $[(H^{13}CO_2)\mathbf{Co}–OC(O)–\mathbf{Co}(H^{13}CO_2)]$, with either a formate ion (Fig. S2.7 A) or the bridging CO_2 ligand (Fig. S2.7 B) hydrogen bonded to the HN groups of an HMD ligand. Another dimer structure contains one CO_2 molecule and one formate ion as the sixth ligands of the metal centers, $[(CO_2)\mathbf{Co}–OC(O)–\mathbf{Co}(H^{13}CO_2)]^+$, with either the bridging CO_2 (Fig. S2.8 A) or peripheral CO_2 (Fig. S2.8 B) being hydrogen bonded to an HMD ligand. While variations in hydrogen bonding do not appear to have a significant effect on the stability of the isomers of each species, the $[(CO_2)\mathbf{Co}–OC(O)–\mathbf{Co}(H^{13}CO_2)]^+$ species is about 8 kcal/mol more stable than $[(H^{13}CO_2)\mathbf{Co}–OC(O)–\mathbf{Co}(H^{13}CO_2)]$.

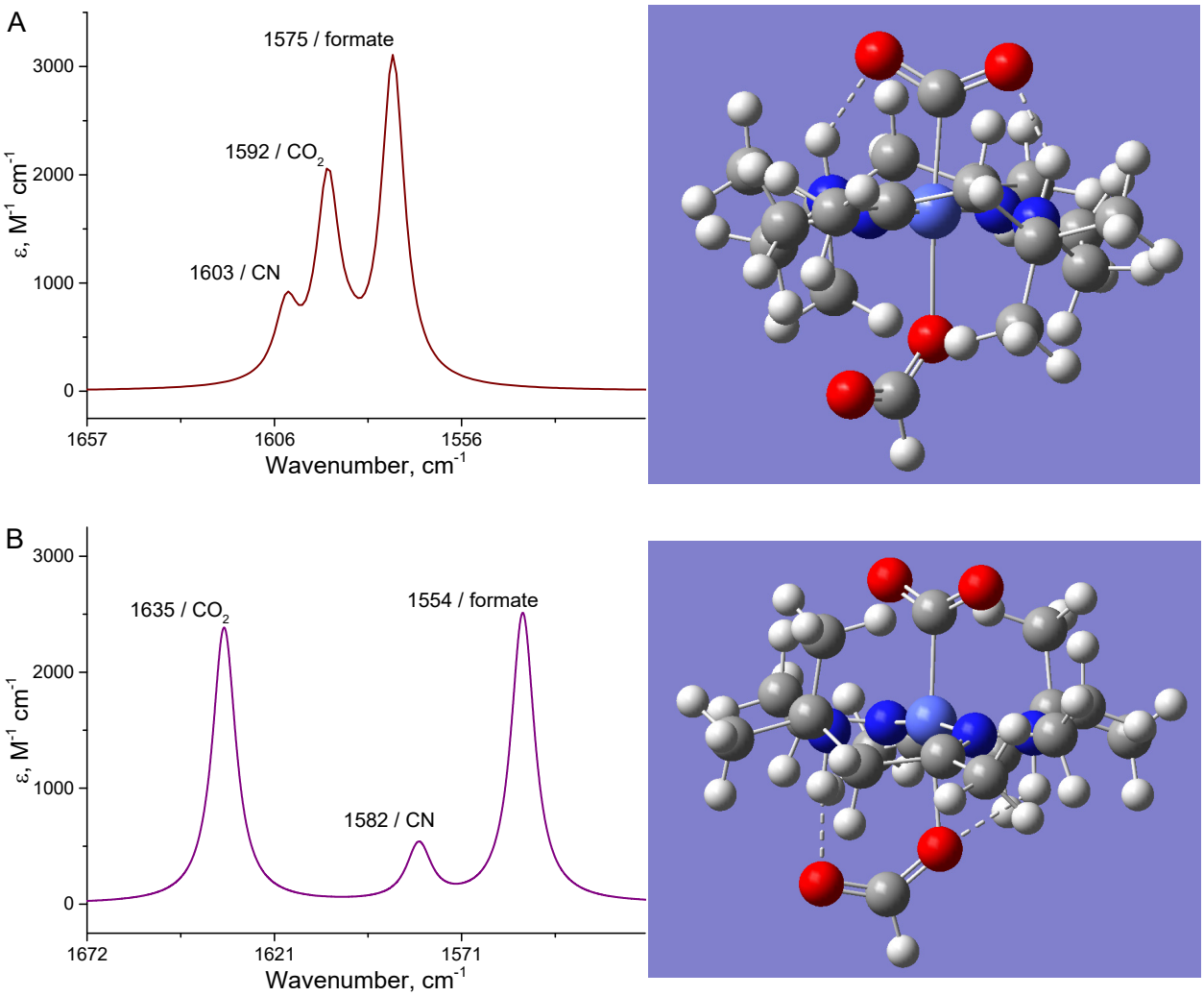

Fig. S2.6. DFT-calculated structures (in CH_3CN) and their corresponding IR spectra (scaled by 0.934) of [**Co**(CO_2)($H^{13}CO_2$)]. Isomers with hydrogen-bonded CO_2 (A) and formate (B) are shown. The calculated free energy of the isomer in panel A is 2.5 kcal/mol higher compared to the isomer in panel B.

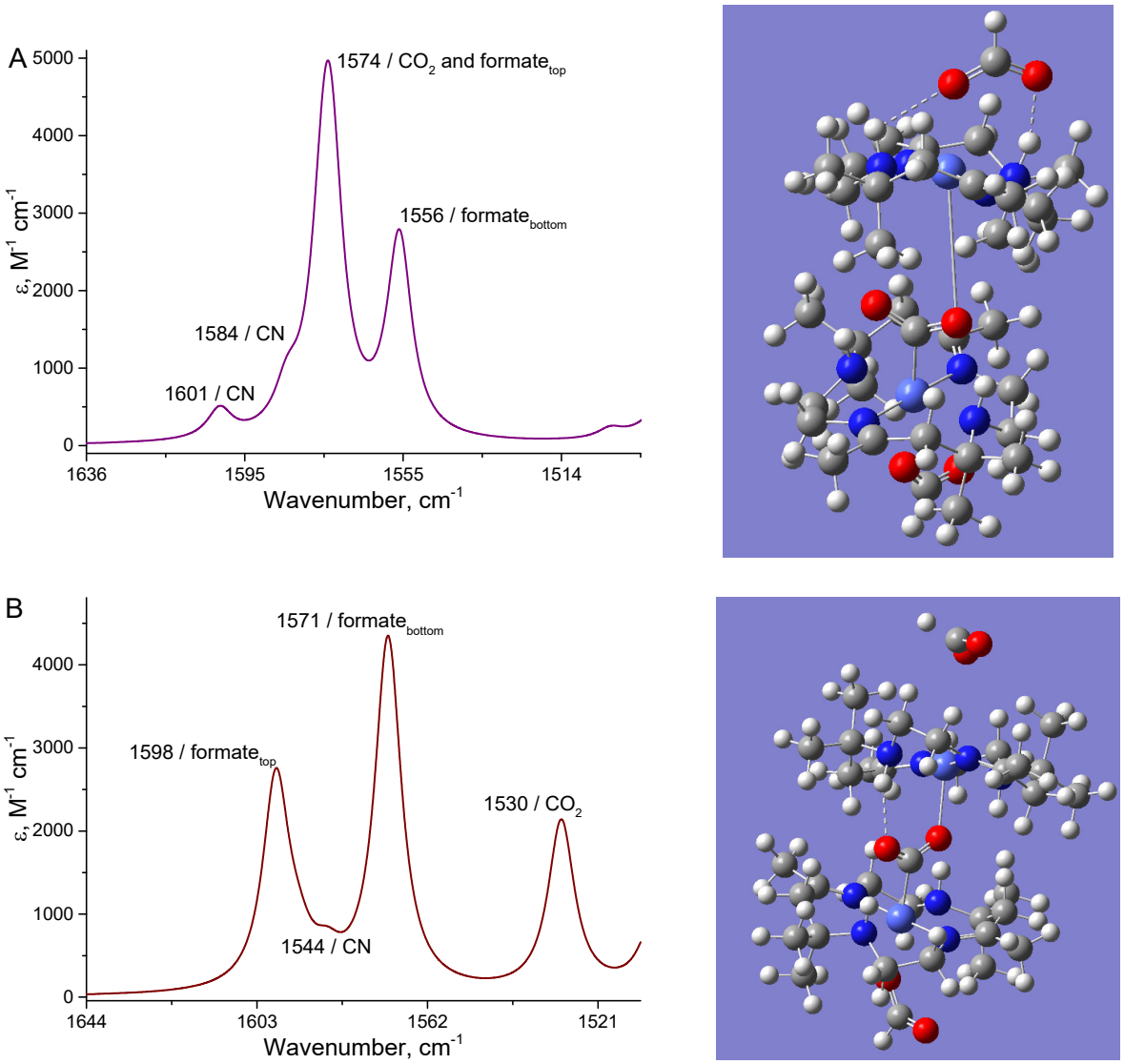

Fig. S2.7. DFT-calculated structures (in CH_3CN) and their corresponding IR spectra (scaled by 0.934) of $[(H^{13}CO_2)\mathbf{Co}–OC(O)–\mathbf{Co}(H^{13}CO_2)]$. Isomers with the hydrogen-bonded formate species $[(^{HB}H^{13}CO_2)\mathbf{Co}–OC(O)–\mathbf{Co}(H^{13}CO_2)]$ (A) and the hydrogen-bonded bridged-CO_2 species $[(H^{13}CO_2)\mathbf{Co}–OC(O)^{HB}–\mathbf{Co}(H^{13}CO_2)]$ (B) are shown. The calculated free energy of the isomer in panel A is 3 kcal/mol higher compared to the isomer in panel B.

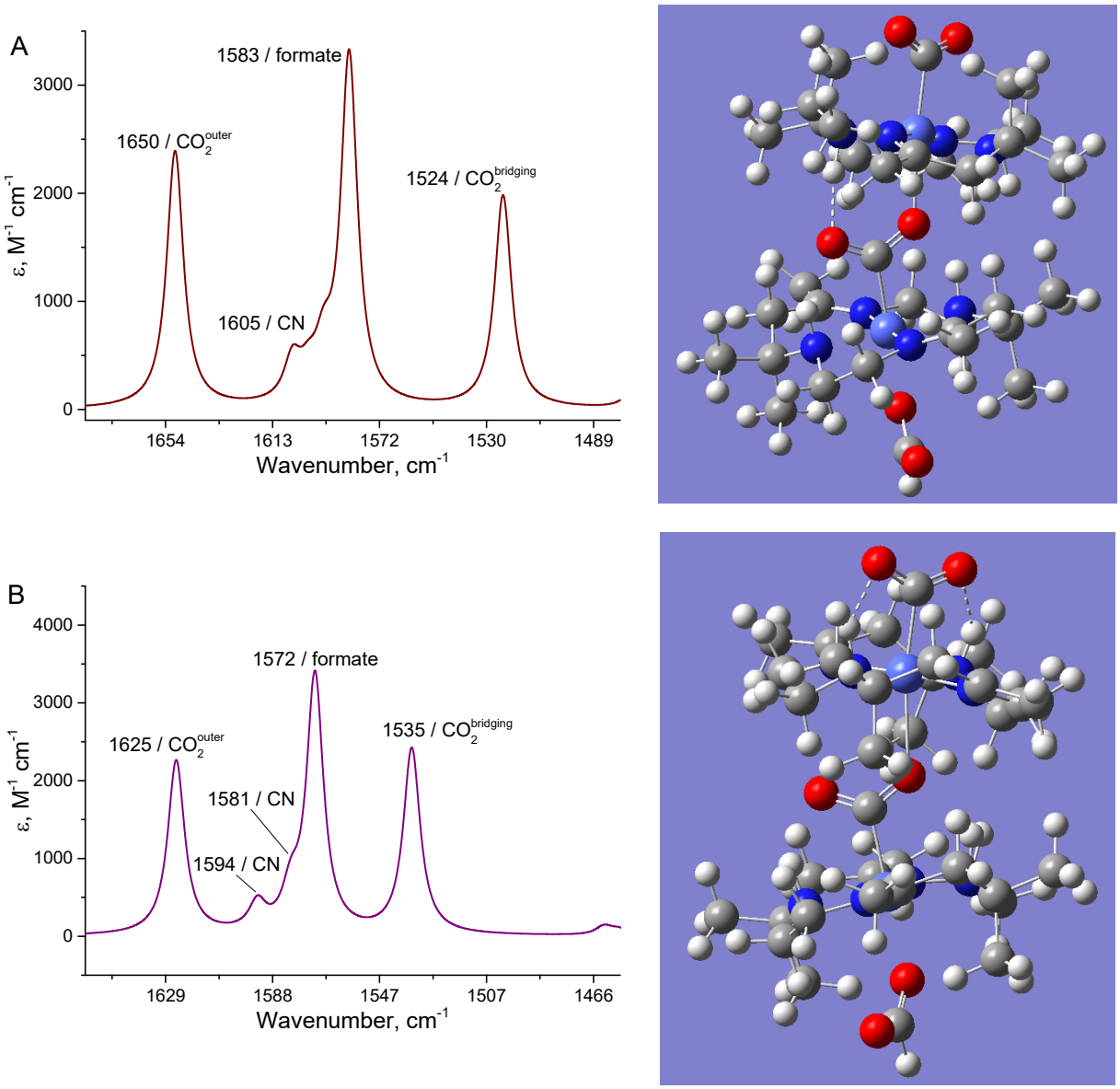

Fig. S2.8. DFT-calculated structures (in CH_3CN) and their corresponding IR spectra (scaled by 0.934) of $[(CO_2)\mathbf{Co}–OC(O)–\mathbf{Co}(H^{13}CO_2)]^+$. Isomers with the hydrogen-bonded bridging CO_2 species $[(CO_2)\mathbf{Co}–OC(O)^{HB}–\mathbf{Co}(H^{13}CO_2)]^+$ (A) and the hydrogen-bonded outer-CO_2-coordinated species $[(^{HB}CO_2)\mathbf{Co}–OC(O)–\mathbf{Co}(H^{13}CO_2)]^+$ (B) are shown. The calculated free energy of the isomer in panel A is 2 kcal/mol higher compared to the isomer in panel B.

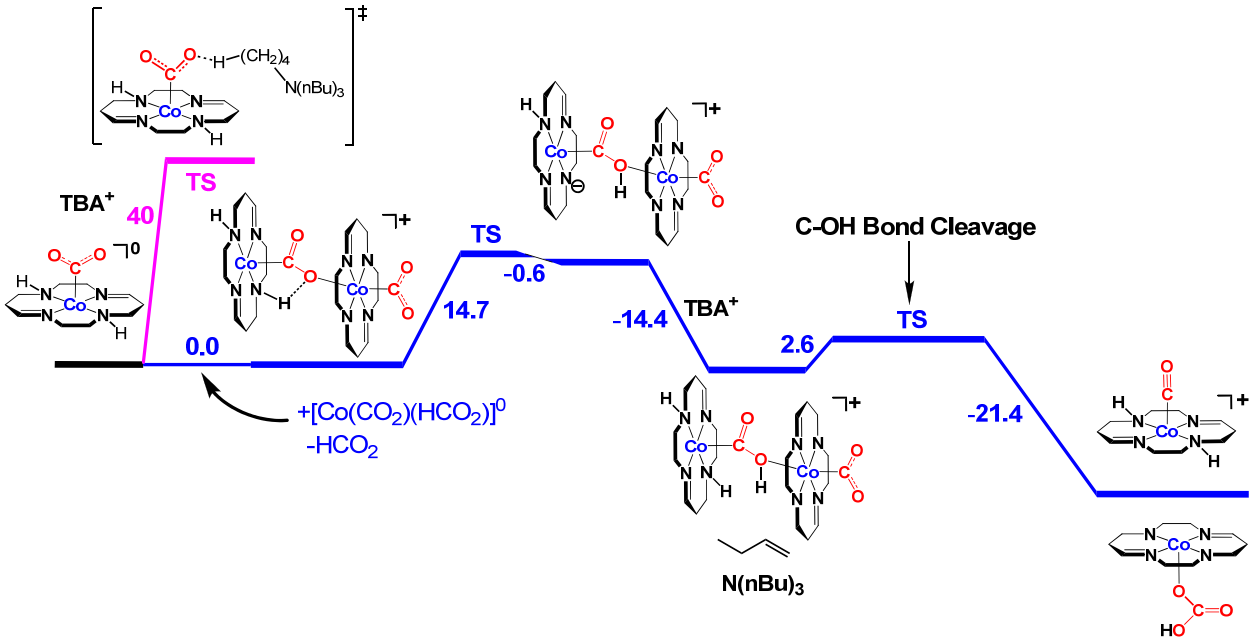

Fig. S2.9. Elementary steps of the transformation of [**Co**$(CO_2)]^0$ and [(CO_2)**Co**–OC(O)–**Co**]$^+$ intermediates into [Co(CO)]$^+$ by their direct protonation with TBA^+, as predicted by DFT calculations. Free energy changes between intermediates and selected transition states are in units of kcal/mol.

Section S3. Pulse radiolysis of [**Co**(CO_2)(HCO_2)] and [(CO_2)**Co**–OC(O)–**Co**(HCO_2)]$^+$

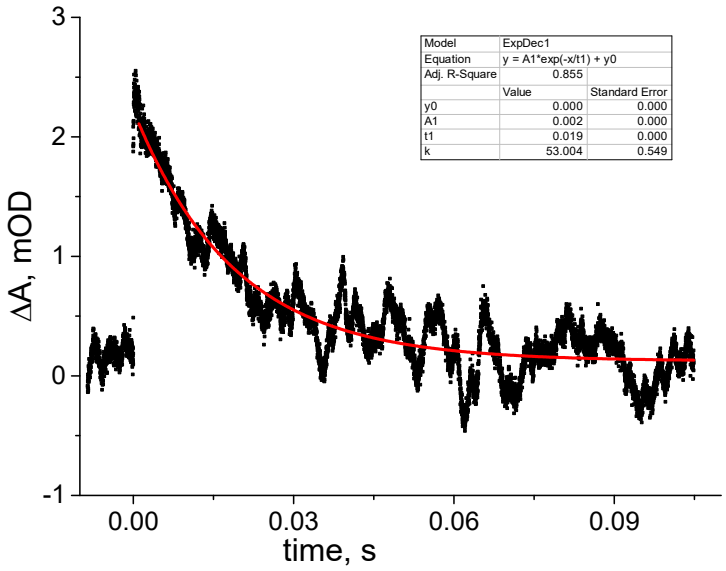

Fig. S3.1. Kinetic decay trace measured at 1216 cm^{-1} for an intermediate formed following pulse radiolysis of a rapidly mixed solution of [**Co**]$^+$ (2 mM after mixing), CO_2 (70 mM after mixing), and [TBA]$^+$[HCO_2]$^-$ (50 mM after mixing), in dry CH_3CN.

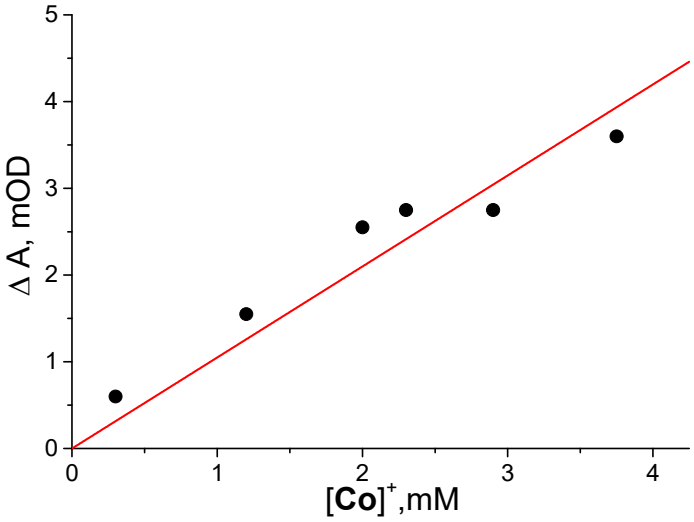

Fig. S3.2. Amplitude of the initial fast component of the growth of the 1917 cm^{-1} band of [**Co**(CO)]$^+$ generated following pulse radiolysis of rapidly mixed solutions of [**Co**]$^+$, CO_2 (70 mM after mixing), and [TBA]$^+$[HCO_2]$^-$ (50 mM after mixing), in dry CH_3CN, plotted vs. the concentration of the [**Co**(CO_2)(HCO_2)] complex that is formed immediately upon mixing. The red line is a linear fit with a fixed intercept at the origin.

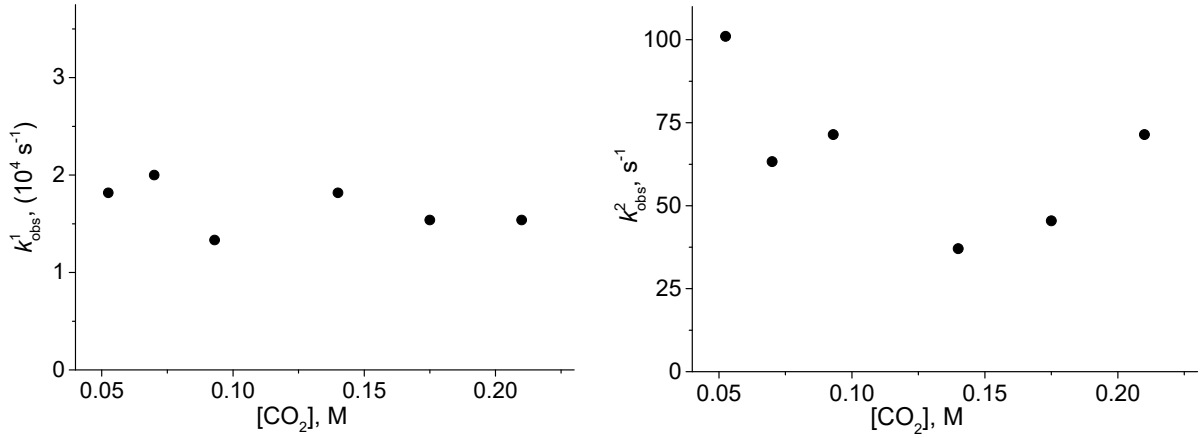

Fig. S3.3. Observed rates of the fast (left) and slow (right) components of the growth of the 1917 cm^{-1} band of [**Co**(CO)]$^+$ generated following pulse radiolysis of rapidly mixed solutions of [**Co**]$^+$ (2 mM after mixing), CO_2, and [TBA]$^+$[HCO_2]$^-$ (50 mM after mixing), in dry CH_3CN, plotted vs. the final concentration of CO_2 obtained after mixing

Section S4. Photocatalytic CO_2 reduction.

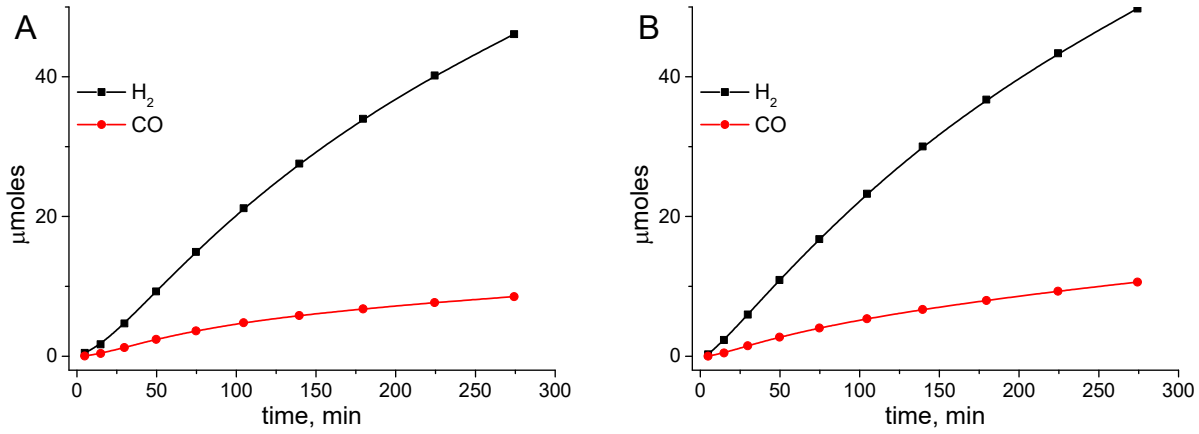

Fig. S4.1. Photolysis of 1 mM [**Co**]$^{2+}$ in dry CH_3CN in the presence of 1 mM *p*-terphenyl and 0.1 M TEA under filtered (> 300 nm) Xe lamp illumination and CO_2 saturation and (A) 50 mM $[TBA]^+[HCO_2]^-$ or (B) 50 mM $[TBA]^+[PF_6]^-$.

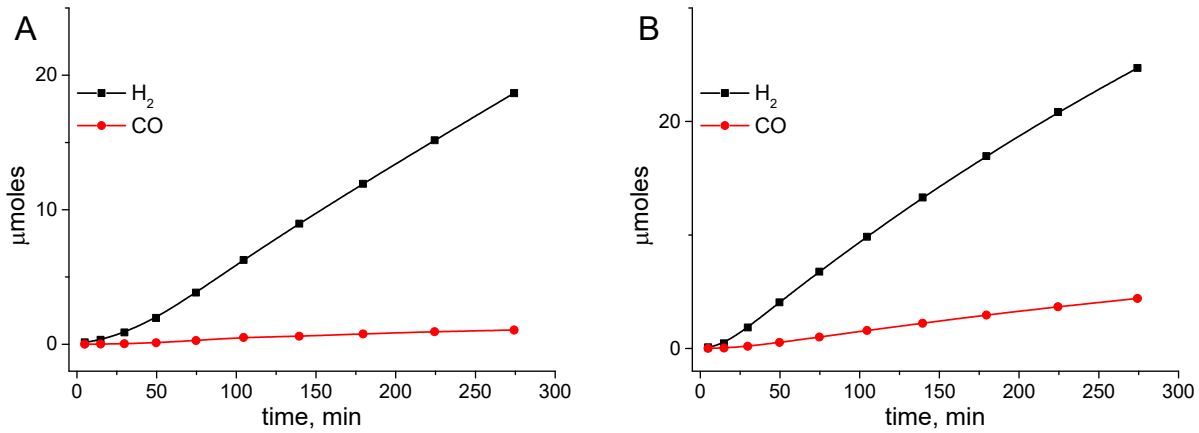

Fig. S4.2. Photolysis of 4 mM [**Co**]$^{2+}$ in dry CH_3CN in the presence of 1 mM *p*-terphenyl and 0.1 M TEA under filtered (> 300 nm) Xe lamp illumination and CO_2 saturation and (A) 50 mM $[TBA]^+[HCO_2]^-$ or (B) 50 mM $[TBA]^+[PF_6]^-$.

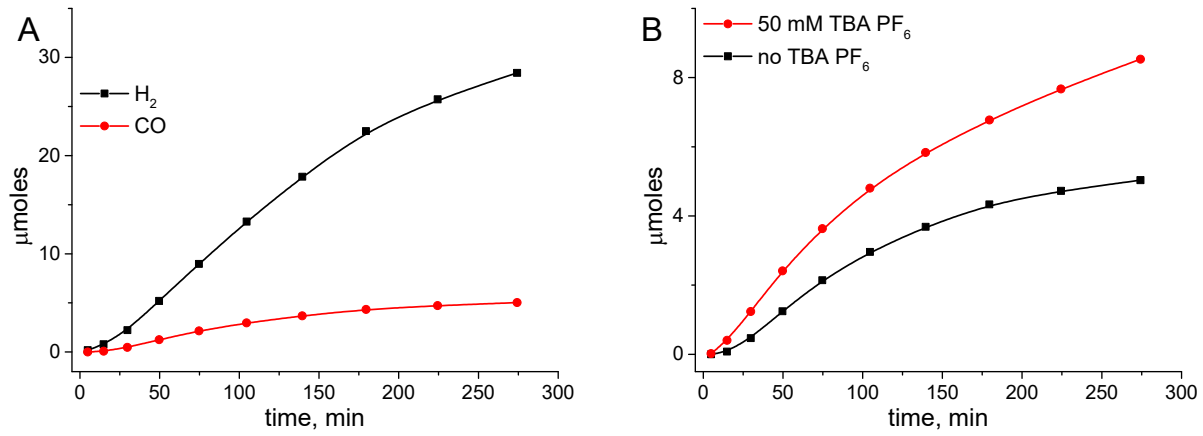

Fig. S4.3. (A) Photolysis of 1 mM $[\mathbf{Co}]^{2+}$ in dry CH_3CN in the presence of 1 mM *p*-terphenyl and 0.1 M TEA under filtered (> 300 nm) Xe lamp illumination and CO_2 saturation without electrolyte added. (B) Comparison of CO yields at 1 mM $[\mathbf{Co}]^{2+}$ without and with 50 mM $[TBA]^+[PF_6]^-$.

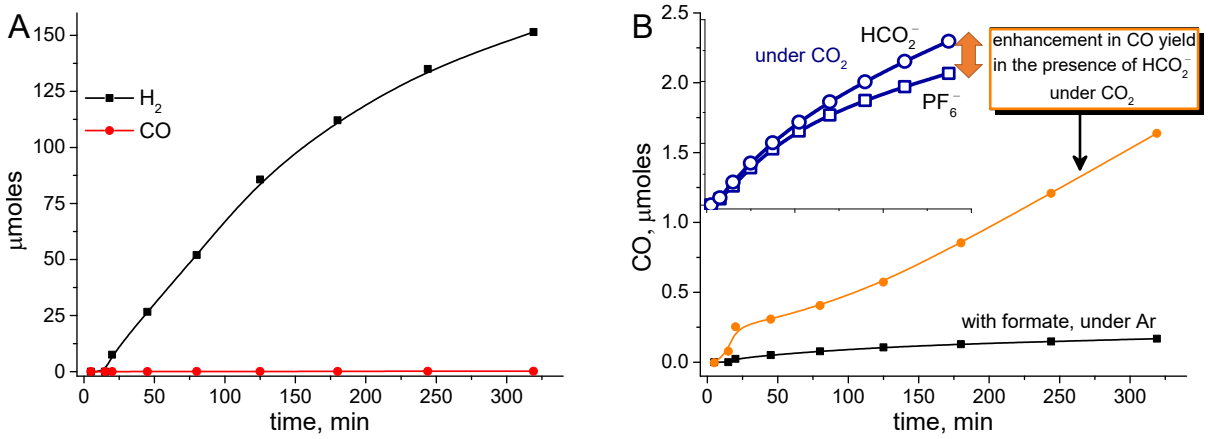

Fig. S4.4. (A) Photolysis of 1 mM $[\mathbf{Co}]^{2+}$ in dry CH_3CN in the presence of 1 mM *p*-terphenyl and 0.1 M TEA and 50 mM $[TBA]^+[HCO_2]^-$ under filtered (> 300 nm) Xe lamp illumination in Ar saturated solution (no CO_2 added). (B) Comparison of enhancement of CO yields upon changing from $[PF_6]^-$ to $[HCO_2]^-$ (orange trace, calculated as a difference of the two traces shown in the insert) in the presence of CO_2, and CO yields from the experiment described in (A) in the absence of CO_2.

Section S5. References

1. Szalda, D. J.; Schwarz, C. L.; Endicott, J. F.; Fujita, E.; Creutz, C., Solution studies of the Cobalt(II) N-rac-CoL^{2+} and N-meso-CoL^{2+} isomers and molecular and crystal structures of the low-spin, 5-coordinate Cobalt(II) macrocyclic complexes N-rac-$CoL(H_2O)(ClO_4)_2$ (1) and N-rac-$CoL(OClO_3)ClO_4$ (2) (L = 5,7,7,12,14,14-hexamethyl-1,4,8,11-tetraazacyclotetradeca-4,11-diene). *Inorg. Chem.* **1989,** *28*, 3214-3219.
2. Fujita, E.; Creutz, C., C-H bond activation by Cobalt(I) macrocycles: rapid H/D exchange between macrocycle and acetonitrile solvent. *Inorg. Chem.* **1994,** *33*, 1729-1730.
3. Szalda, D. J.; Fujita, E.; Creutz, C., Cobalt(I), Cobalt(II), and Cobalt(III) complexes of a tetraaza 14-membered macrocycle, 5,7,7,12,14,14-hexamethyl-1,4,8,11-tetraazacyclotetradeca-4,11-diene (L) - crystal and molecular-structures of $[CoL(Co)]ClO_4$, trans-$CoLCl_2$, and cis-$[CoL(CO_3)]ClO_4$. *Inorg. Chem.* **1989,** *28*, 1446-1450.
4. Fujita, E.; Creutz, C.; Sutin, N.; Szalda, D. J., Carbon dioxide activation by Cobalt(I) macrocycles - factors affecting CO_2 and Co binding. *J. Am. Chem. Soc.* **1991,** *113*, 343-353.
5. Fujita, E.; Furenlid, L. R.; Renner, M. W., Direct XANES evidence for charge transfer in Co-CO_2 complexes. *J. Am. Chem. Soc.* **1997,** *119*, 4549-4550.
6. Fujita, E.; Creutz, C.; Sutin, N.; Brunschwig, B. S., Carbon dioxide activation by cobalt macrocycles - evidence of hydrogen-bonding between bound CO_2 and the macrocycle in solution. *Inorg. Chem.* **1993,** *32*, 2657-2662.
7. Fujita, E.; Creutz, C.; Sutin, N.; Brunschwig, B. S., CARBON-DIOXIDE ACTIVATION BY COBALT MACROCYCLES - EVIDENCE OF HYDROGEN-BONDING BETWEEN BOUND CO2 AND THE MACROCYCLE IN SOLUTION. *Inorg. Chem.* **1993,** *32*, 2657-2662.
8. Cheng, S. C.; Blaine, C. A.; Hill, M. G.; Mann, K. R., Electrochemical and IR Spectroelectrochemical Studies of the Electrocatalytic Reduction of Carbon Dioxide by [Ir2(dimen)4]2+ (dimen = 1,8-Diisocyanomenthane). *Inorg. Chem.* **1996,** *35*, 7704-7708.
9. Fujita, E.; Szalda, D. J., Crystallization and structure of a binuclear species containing the Co-C(OH)-O-Co moiety. *Inorg. Chim. Acta* **2000,** *297*, 139-144.